Crystallisation process of hybrid halide perovskites: in-situ perception of the crystallisation path

A Dissertation
Submitted in Partial Fulfilment of the Requirements for the Degree of
Doctor rerum naturalium (Dr. rer. nat.)

to the Department of Earth Sciences
of Freie Universität Berlin

by
Ana Palacios Saura

Berlin, 2024

First examiner: Prof. Dr. Susan Schorr

Second examiner: Prof. Dr. Andreas Taubert

Date of defence: 6th February 2025

“Lemons”

- *Ana P. & David M.*

Eidesstattliche Erklärung

Ich erkläre hiermit, dass ich die vorliegende „Crystallisation process of hybrid halide perovskites: in-situ perception of the crystallisation path“ selbstständig und ohne Benutzung anderer als der angegebenen Quellen und Hilfsmittel angefertigt habe. Ferner wird hiermit erklärt, dass die Dissertation weder in der vorgelegten noch in einer ähnlichen Fassung zu einem früheren Zeitpunkt an der Freien Universität oder einer anderen Hochschule als Dissertation eingereicht worden ist.

Teile dieser Dissertation wurden in MRS Communications veröffentlicht (siehe Referenz 75, The big bang of halide perovskites: The starting point of crystallization. *MRS Commun.* 14, 711–716 (2024), DOI: 10.1557/s43579-024-00611-x).

A. Palacios Saura: Konzeptualisierung, Untersuchung, Datenanalyse, Schreiben des Skriptes (ursprünglicher Entwurf). J. Breternitz: Konzeptualisierung, Betreuung, Modellierungen (DFT-Berechnungen) und Überarbeitung. A. Hoell: Durchführen der Messung (SAXS) und Überarbeitung. S. Schorr: Konzeption, Betreuung, Beschaffung von Finanzmitteln, Begutachtung und Redaktion. Alle Autoren haben die veröffentlichte Fassung des Manuskripts gelesen und ihr zugestimmt.

Berlin, 02.09.2024

Ana Palacios Saura

Acknowledgements

First, I would like to acknowledge my supervisor, Prof. Dr. Susan Schorr, for her support and patience during this PhD and her words of encouragement. I would also like to thank Prof. Dr. Joachim Breternitz, for his help and support while he was my daily supervisor.

I would like to express my gratitude to Dr. Armin Hoell, Dr. Uwe Keiderling, Niyaz Huseyn-Zada for helping me with the SAXS measurements. Thanks to the Physikalisch-Technische Bundesanstalt for allocating time for my measurements.

In addition, I would like to show my gratitude to the Helmholtz International Research School "Hybrid Integrated Systems for Conversion of Solar Energy" (HI-SCORE) for the funding for this project.

Finally, I would like to acknowledge all my colleagues at the Structure Dynamics of Energy Materials department for the good times and for creating an enjoyable work environment. I would like to give special thanks to Dr Galina Gurieva for her immense support, fruitful talks and all her help, despite not being my official second supervisor. I would also like to thank Dr Michael Tovar for organising the work outings and all the social events, especially for being the backup when the canteen is closed. Thanks to Henrik Prell for all the interesting discussions and talks. Also, special thanks to Juanita Hidalgo for her encouragement and good times during her stay in Berlin. And last but not least, I would like to thank David Matzdorff for turning from a colleague to a very good friend.

Not to forget, my deepest gratitude to my parents and brother Amador, Angela and Angel for their continuous support not only during the PhD but during my whole life and to Kristian, für alles <3

Abstract

The effects of climate change are becoming more frequent and extreme; effects such as droughts, floods, heat and cold waves are putting the lives of millions of people at risk. The main contributor to climate change is the use of fossil fuels such as coal, oil and gas;[1] hence, there is a need to replace that source of energy with renewable energy. Solar energy is the third most used renewable energy, after hydropower and wind energy. The material that is mostly used for solar cells is silicon due to its high efficiency and stability; however, its production is expensive and highly energy-consuming. In the last years, other materials[2,3] have risen to offer a more sustainable approach, but despite their many advantages, they cannot compete in terms of efficiency. Hybrid halide perovskites (HHPs) have drawn the attention of the scientific community, not only for their steep increase in power conversion efficiency during the last decade, up to 26.7%[4] in 2024 but also for using low-cost solution-based processing methods. Despite their popularity, it is not yet fully understood what the formation mechanism of HHPs is. This work aims to bring more clarity on how HHPs form from solution, focusing on how the solvent used interacts with the precursors before the perovskite is formed. For this reason, the precursor solution of $MAPbI_3$ ($MA= CH_3NH_3$) was studied with 4 common solvents used to produce perovskite layers: γ-butyrolactone (GBL), N,N-dimethylformamide (DMF), N-Methyl-2-pyrrolidone (NMP), dimethyl sulfoxide (DMSO) and mixtures thereof. Furthermore, since HHPs present changes in the bandgap when the composition is modified,[5] the effect of substituting I^- for Br^- and Cl^- and substituting MA^+ for FA^+ ($HC(NH_2)_2$) and alkali metals (Na^+, K^+, Rb^+, Cs^+) was studied as well. Small angle X-ray scattering was the method of choice to investigate the precursor solutions since it can determine the size, shape, interaction, and average distance between the scattering objects in solutions in the range of 0.5 – 100 nm. The results obtained from SAXS can be explained by a core-shell model, where the core is a $[PbI_6]$, which can be arranged as a single octahedron or as a corner-sharing octahedra and the shell is formed by randomly oriented

solvent molecules. When the A-cation is molecular (FA^+, MA^+), it has no influence on the arrangement of the scattering objects, but when the A-cation is inorganic, the $[PbI_6]$ octahedra of adjacent scattering objects are surrounded by a solvent shell with molecules or by an A-cation shell. The results from SAXS showed higher polydispersity in the samples with an inorganic A-cation, which is in agreement with the proposed model. Changing the I^- for Br^- favours the single octahedron arrangement in the core, whereas when Cl^- is used as a halide, there is no evidence of agglomeration in the precursor solution.

Zusammenfassung

Die Auswirkungen des Klimawandels werden immer häufiger und extremer; Dürren, Überschwemmungen, Hitze- und Kältewellen gefährden das Leben von Millionen von Menschen. Der Hauptverursacher des Klimawandels ist die Nutzung fossiler Brennstoffe wie Kohle, Öl und Gas.[1] Daher besteht die Notwendigkeit, diese Energiequellen durch erneuerbare Energien zu ersetzen. Die Solarenergie ist nach der Wasserkraft und der Windenergie die am dritthäufigsten genutzte erneuerbare Energie. Das am häufigsten für Solarzellen verwendete Material ist Silizium, da es einen hohen Wirkungsgrad und eine hohe Stabilität aufweist; seine Herstellung ist jedoch teuer und sehr energieaufwändig. In den vergangenen Jahren sind weitere Materialien[2,3] auf den Markt gekommen, die einen nachhaltigeren Ansatz bieten, aber trotz ihrer vielen Vorteile bezüglich ihrer Effizienz nicht mithalten können. Hybrid-Halogenid-Perowskite (HHP) haben die Aufmerksamkeit der wissenschaftlichen Gemeinschaft auf sich gezogen, nicht nur wegen ihres steilen Anstiegs des Wirkungsgrads bei der Energieumwandlung in den letzten zehn Jahren (bis zu 26,7%[4] im Jahr 2024), sondern auch wegen der Verwendung kostengünstiger lösungsbasierter Verarbeitungsmethoden. Trotz ihrer Beliebtheit ist der Entstehungsmechanismus von HHP noch nicht vollständig erforscht. Diese Arbeit zielt darauf ab, mehr Klarheit darüber zu schaffen, wie sich HHPs aus einer Lösung bilden, und konzentriert sich darauf, wie das verwendete Lösungsmittel mit den Vorstufen interagiert, bevor der Perowskit gebildet wird. Aus diesem Grund wurde die Vorläuferlösung von $MAPbI_3$ ($MA^+ = CH_3NH_3^+$) mit vier gängigen Lösungsmitteln untersucht, die zur Herstellung von Perowskit-Schichten verwendet werden: γ-Butyrolacton (GBL), N,N-Dimethylformamid (DMF), N-Methyl-2-pyrrolidon (NMP), Dimethylsulfoxid (DMSO) und Mischungen davon. Da sich bei HHPs die Bandlücke ändert, wenn die Zusammensetzung angepasst wird,[5] wurde auch die Wirkung des Ersatzes von I^- durch Br^- und Cl^- und des Ersatzes von MA^+ durch FA^+ ($HC(NH_2)_2^+$) und Alkalimetalle (Na^+, K^+, Rb^+, Cs^+) untersucht. Für die Untersuchung der Vorläuferlösungen war die Kleinwinkel-Röntgenstreuung die Methode der Wahl, da sie die

Größe, Form, Wechselwirkung und den durchschnittlichen Abstand zwischen den Streuobjekten in Lösungen im Bereich von 0,5 - 100 nm bestimmen kann. Die mit SAXS erzielten Ergebnisse lassen sich durch ein Kern-Schale-Modell erklären, bei dem der Kern ein [PbI_6] ist, das als einzelner Oktaeder oder als eckenteilender Oktaeder angeordnet sein kann und die Schale von zufällig orientierten Lösungsmittelmolekülen gebildet wird. Wenn das A-Kation molekular ist (FA^+, MA^+), hat es keinen Einfluss auf die Anordnung der Streuobjekte. Bei einem anorganischen A-Kation hingegen, sind die [PbI_6]-Oktaeder benachbarter Streuobjekte von einer Lösungsmittelschale mit Molekülen oder von einer A-Kationenschale umgeben. Die SAXS-Ergebnisse zeigten eine höhere Polydispersität in den Proben mit einem anorganischen A-Kation, was mit dem vorgeschlagenen Modell übereinstimmt. Der Austausch von I^- gegen Br^- begünstigt die Anordnung eines einzelnen Oktaeders im Kern, während bei Verwendung von Cl^- als Halogenid keine Anzeichen für eine Agglomeration in der Vorläuferlösung zu erkennen sind.

Contents

List of abbreviations

2θ	diffraction angle
μ	location parameter (median of size distribution)
A	scale factor
A-cation	cation in the A-site of ABX_3 structure
ACN	acetonitrile
B-cation	cation in the B-site of ABX_3 structure
d_{exp}	experimental distance
DMF	N,N-dimethylformamide
d_{model}	modelled distance between scattering objects
DMSO	dimethyl sulfoxide
DN	Guttmann's donor number
E_g	bandgap
FA	formamidinium
FAI	formamidinium iodide
$FAPbI_3$	formamidinium lead iodide
FCM	four crystal monochromator
f_p	volume fraction
GBL	γ-butyrolactone
HHP	hybrid halide perovskite
HI	hydroiodic acid
ITC	inverse temperature crystallisation
MA	methylammonium
MAI	methylammonium iodide
$MAPbBr_3$	methylammonium lead bromide
$MAPbCl_3$	methylammonium lead chloride
$MAPbI_3$	methylammonium lead iodide
N(r)	size distribution
NMP	N-Methyl-2-pyrrolidone
NREL	national renewable energy lab
p	shape parameter
P(q)	form factor
$PbBr_2$	lead bromide
$PbCl_2$	lead chloride

PbI_2	lead iodide
PCE	power conversion efficiency
PSC	perovskite solar cell
PTB	Physikalisch-Technische Bundesanstalt
PV	photovoltaic
q	scattering vector
q_{max}	scattering vector at maximum intensity
r	radius
$r_{A-cation}$	radius A-cation
$r_{core}^{corner-sharing}$	radius of $[Pb_2X_{11}]^{7-}$ arranged as corner-sharing octahedra
R_G	radius of gyration
R_{HS}	radius of the hard sphere
$\bar{r}_s$	geometrical mean of solvent radii
r_{s1}	shortest solvent radius
r_{s2}	medium solvent radius
r_{s3}	longest solvent radius
r_s^{app}	apparent radius
r_{shell}	radius shell
r_{core}^{single}	radius of $[PbX_6]$ arranged as a single octahedron
r_{X^-}	radius halide
S(q)	structure factor
SAXS	small angle X-ray scattering
$V_p(r)$	volume of one particle
X-halide	halide in the X-site of ABX_3 structure
XRD	X-ray diffraction
α-phase	cubic phase
β-phase	tetragonal phase
γ-phase	orthorhombic phase
δ-phase	delta phase, non-perovskite
$\Delta\rho$	scattering length density difference
λ	wavelength
ρ	scattering length density
σ	polydispersity index

List of figures

List of tables

Chapter 1. Introduction

1.1. The sun as an energy source

The need for renewable energies is more important than ever due to the rise of energy costs as well as the climate change consequences, such as floods, droughts and extreme temperatures. The sun is a vital component which can provide an almost limitless supply of clean energy. The use of photovoltaic (PV) technology to harvest solar energy opens the door to meeting the world's energy demand with free renewable energy. The Sun can provide up to 173000 TWh per year, which is enough to provide clean energy for the whole world compared to the energy consumption on Earth in 2022, which was 167788 TWh.[1,6]

Since the first solar cell was developed by Bell Labs in 1954, with an efficiency of 6%,[7] it has been a constant race to produce materials which can absorb sunlight more efficiently. In 1961, Shockley and Queisser developed a model which predicts the theoretical limit for maximum power conversion efficiency (PCE) for single junction solar cells (Figure 1.1).[8] Silicon is the most popular material for solar cells. However, it is approaching its practical limit (29%). The need to surpass the practical limit to be closer to the theoretical limit (33%) and to lower the solar cell production cost inspired the scientific community to look for other materials to be used as absorbers for solar cells (emerging PV). Emerging PV materials, like hybrid halide perovskites, provide low-cost and low-temperature solution based synthesis methods together with a record efficiency of 26.7%.[4] These are very promising materials, however, their lack of long-term stability makes it difficult to be commercialised at a large scale.

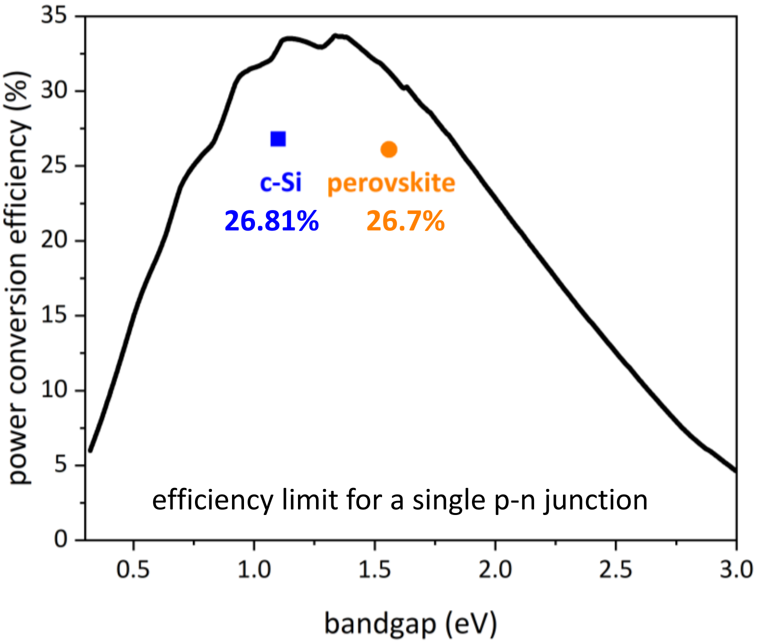

Figure 1.1. Efficiency limit for a single p-n junction according to the Shockley-Queisser limit.[8] The maximum efficiencies achieved with silicon and hybrid halide perovskites solar cells are highlighted.

1.2. HHPs as an absorber material for solar cells

The use of HHPs as an absorber material for solar cells is relatively new. In 2009, Kojima et al.[9] reported the first solar cell using $MAPbI_3$ as an absorber material obtaining 3.81% efficiency. As of August 2024, the last reported record efficiency in perovskite-based solar cells is 26.7%,[4] which is nearly the practical limit of silicon-based solar cells, at 29%.[10]

The mineral perovskite ($CaTiO_3$, Figure 1.2) was discovered in Russia in 1839 by Gustav Rose and named after Count Lev Alekseyevich von Perovski, who was a Russian mineralogist and politician.[11] The noun perovskite not only refers to the mineral but it is also applied to the compounds which crystallise in the same structure.

HHPs have an ABX_3 composition and crystallise in the perovskite-type structure, where A is a monovalent organic cation, typically methylammonium (MA^+) or formamidinium (FA^+), B is a divalent metallic cation such as Pb^{2+} or Sn^{2+}, and X is a halide, I^-, Br^- or Cl^-. For a compound to be considered part of the perovskite family, certain requirements must be fulfilled. It must have an A:B:X composition ratio of 1:1:3; the B-cation must be octahedrally coordinated to the anion, and they must be organised in a 3D network of corner-sharing octahedra.[12]

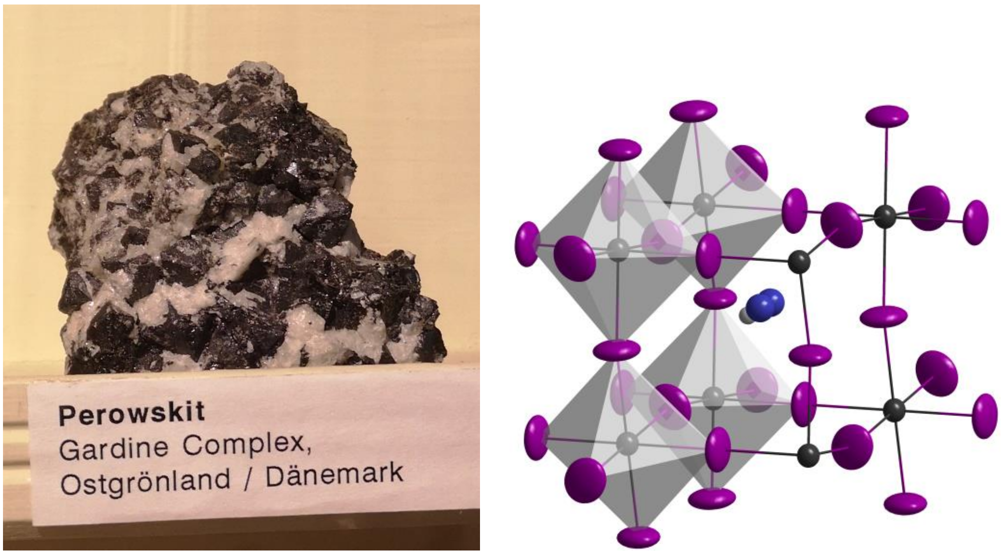

Figure 1.2. Mineral perovskite at the Museum für Naturkunde in Berlin (left). Example of tetragonal $MAPbI_3$. The black balls represent Pb^{2+}, the purple ellipsoids represent I^- and the blue and white balls represent MA^+ (right).

HHPs can crystallise in the cubic aristotype (space group $P\bar{3}cm$), or the lower symmetry hettotypes tetragonal (space group $I4cm$) or orthorhombic (space group $Pnma$). In case of $MAPbI_3$, the phase transitions occur at 330 K (cubic → tetragonal phase transition) and at 161 K (tetragonal → orthorhombic phase transition) (Figure 1.3).

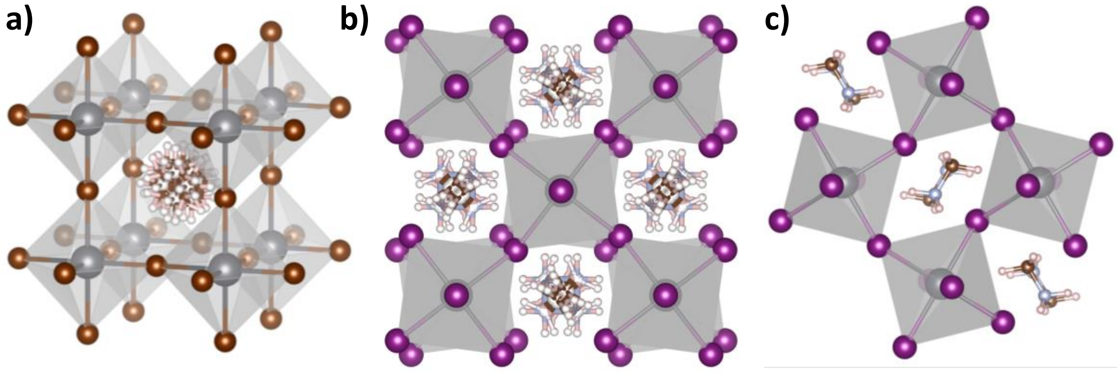

Figure 1.3. $MAPbI_3$ modifications a) above 330 K, cubic; b) 330 – 161 K, tetragonal; c) below 161 K, orthorhombic. Visuals made with VESTA.[13]

HHPs are suitable as absorber materials in solar cells for several reasons. Their high absorption coefficient[14] allows HHPs to absorb sunlight in the visible spectrum even on thin films. The bandgap energy of HHPs can be tuned when varying their composition by exchanging the anion or the cations[5] making this material ideal for single junction (1.1-1.4 eV) as well as for tandem solar cell applications (1.1-1.7 eV).[15] As an example, the bandgap energy of $MAPb(I_{1-x}Br_x)_3$ can be tuned continuously from 1.56 to 2.3 eV. Another characteristic of HHPs is their charge carriers diffusion length,[16] allowing electrons and holes to move large distances before recombining.

In order to be established in the PV market, a few issues should be overcome. Despite the advances in efficiency in the last years, long-term stability remains an unsolved problem.[17] Not only that, but to implement HHPs at large scale, e.g. 1 TW solar farms, there are not enough materials to cover the demand.[18]

1.3. Motivation of the thesis

HHPs are very popular amongst the scientific community due to the rapid increase of PCE, up to 26.7% in 2024[4] and their ease of processing. However, the syntheses from solution remain the most popular due to their low processing temperature and low cost.[19–21] However, despite their popularity, their formation mechanism is not yet well understood. HHPs are characterised by the possibility of being synthesised by solution at low temperatures.[19–21] Most of the studies have been applied to solid HHPs using XRD, however, it is necessary to understand the formation processes from solution. For this reason, it is necessary to understand what is the effect of the solvent, the anion and the *A*-cation on the scattering objects in solution. $MAPbI_3$ precursor solution synthesised in GBL, DMF, NMP, DMSO and mixtures was investigated with small angle X-ray scattering to explain the role of the solvent. This technique provides information in the nanometre range, which is ideal for studying the agglomerates in the precursor solution. The effect of the anion was studied by comparing $MAPbI_3$, $MAPbBr_3$ an $MAPbCl_3$ precursor solutions synthesised in DMF:DMSO and finally, the effect of the cation was investigated by comparing the effect of organic *A*-cation and inorganic *A*-cation. Additionally, the ageing of $MAPbI_3$, as well as the ageing of $MAPbI_3$ precursor solution, were investigated.

Chapter 2. Experimental

It is possible to synthesise hybrid halide perovskites using a number of techniques. This dissertation focuses on HHPs synthesised from solution, as well as the characterisation of the precursor solution.

2.1. Synthesis of hybrid halide perovskites from solution

For all the synthesis, the chemicals were used as received without further purification.

2.1.1. Antisolvent method

$MAPbI_3$ was synthesised following the antisolvent method (Figure 2.1) presented by Rakita et al.[21] The precursor solution was prepared by mixing 0.7100 g MAI (Tokyo Chemical Industry, 99%) and 2.0699 g PbI_2 (Tokyo Chemical Industry, 99,9985%) in 15 mL acetonitrile (Sigma-Aldrich, 99.5%). $MAPbI_3$ was obtained through the following chemical reaction:

$$CH_3NH_3I + PbI_2 \xrightarrow{ACN,HI} CH_3NH_3PbI_3$$

While stirring the solution, 1.5 mL HI (Sigma-Aldrich, 57 wt% in H_2O, distilled, stabilised 99.95%) was added. The solution was stirred until all the solutes dissolved.

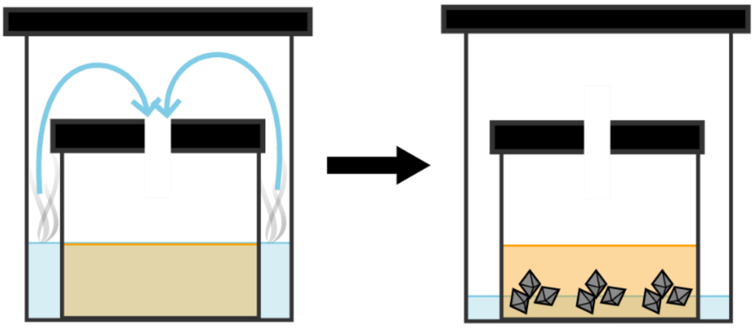

Figure 2.1. Scheme of the antisolvent method.

The solution was transferred into two vials, whose lids had been previously perforated, to allow the antisolvent vapour to enter the vials. After placing the closed vials in a bottle, 15 mL ethyl acetate (ChemCruz, 99%) was added. The bottle was closed and sealed with parafilm. After 48 hours, a yellow precipitate appeared at the bottom of the vials, however, there was no evidence of crystal growth. The vials were left undisturbed for 14 days to let the crystals grow. After that time, crystals formed at the bottom and on the walls of the vials. Together with the $MAPbI_3$ crystals, a large amount of PbI_2 precipitated at the bottom of the vials. The precursor solution was transferred into a crystallisation dish, and the crystals were taken with tweezers. They were dried with a Kimwipe (Kimtech Science) and placed in a vial for further X-ray diffraction (XRD) analysis.

2.1.2. Acetate method

$MAPbI_3$ was synthesised following the acetate method (Figure 2.2) presented by Dang et al.[20] The precursor solution was prepared by introducing 1.9190 g $Pb(CH_3COO)_2 \cdot 3H_2O$ (Roth, 99.5%) in 13 mL HI in an Erlenmeyer Flask. $MAPbI_3$ was obtained through the following chemical reactions:

$$Pb(CH_3COO)_2 + 2HI \longrightarrow PbI_2 + 2CH_3COOH$$
$$CH_3NH_3I + PbI_2 \longrightarrow CH_3NH_3PbI_3$$

The solution was stirred at 65 °C until $PbAc_2 \cdot 3H_2O$ was completely dissolved. While stirring, 0.7997 g MAI were introduced. Once all the precursors were dissolved, the temperature was lowered to 40 °C and the magnetic stirrer was removed to avoid any interference with the crystallisation. The Erlenmeyer flask was covered with a petri dish. After 48 hours, the solution became darker, but there was no sign of crystal growth.

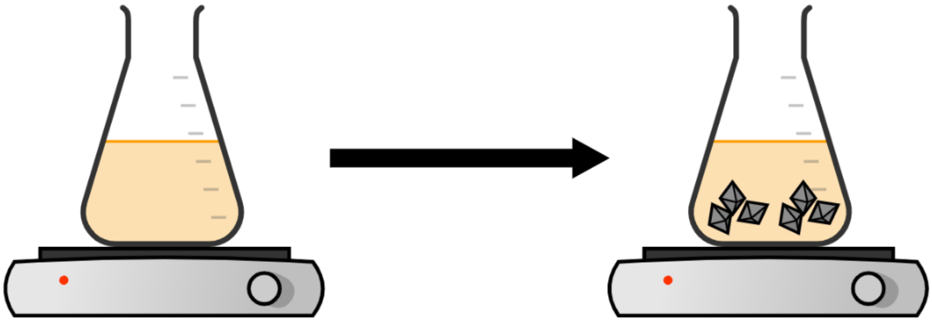

Figure 2.2. Scheme of the acetate method.

The solution was left undisturbed at 40 °C for 14 days, however, no change was observed. The solution was transferred to a crystallisation dish and placed on the heating plate, keeping the temperature at 40 °C. After 2 h, the solvent evaporated and crystals appeared at the bottom of the crystallisation dish. The newly formed $MAPbI_3$ crystals were left in the crystallisation dish to dry on the heating plate for 4 hours. After that time, the crystals were transferred into a vial for further XRD analysis.

2.1.3. Inverse Temperature Crystallisation method

An adaptation of the inverse temperature crystallisation method (ITC, Figure 2.3) presented by Saidaminov et al,[22] was the method of choice to synthesise bulk $MAPbI_3$ as well as the precursor solution of hybrid halide perovskites with different composition.

- **Bulk $MAPbI_3$.** Bulk $MAPbI_3$ was prepared using the following GBL:DMF solvent ratios: 100% GBL, 90:10, 80:20, 70:30, 60:40, 50:50, 40:60, 30:70, 20:80, 10:90 and 100% DMF. The precursor solutions were prepared in a 50 mL round bottom flask by mixing stoichiometric amounts of MAI and PbI_2 in 4 mL of the solvent of choice to obtain a 1.2 M solution. The solution was stirred at 60 °C under a nitrogen atmosphere for 1 h and then transferred into a crystallisation glass. The solution was heated to 100 °C for 60 minutes to evaporate the solvent, obtaining a black powder. The powder was kept in a vial in the glovebox for further XRD analysis.

  $MAPbI_3$ was obtained through the following chemical reaction:

$$CH_3NH_3I + PbI_2 \xrightarrow{solvent} CH_3NH_3PbI_3$$

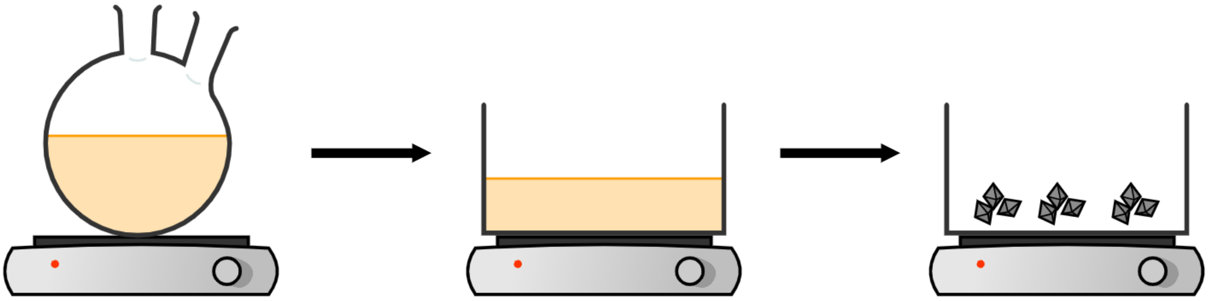

Figure 2.3. Scheme of the inverse temperature crystallisation (ITC) method.

- **$MAPbI_3$ precursor solutions.** $MAPbI_3$ precursor solutions were prepared using GBL, DMF, NMP, DMSO, and mixtures as solvents in different ratios (Table 2.1). The precursor solutions were prepared in a 50 mL round bottom flask by mixing stoichiometric amounts of MAI and PbI_2 in 5 mL of the solvent of choice to obtain a 0.8 M solution. The solution was stirred at 60 °C under a nitrogen atmosphere for 1 h. Samples for further SAXS measurement were taken after 30 and 60 min by introducing a thin (wall thickness of 0.1 mm) rectangular borosilicate capillary (CM Scientific) into the solution.

Table 2.1. Solvent ratios used in the preparation of $MAPbI_3$ precursor solutions.

GBL:DMF	GBL:NMP	GBL:DMSO	DMF:DMSO	NMP:DMSO	DMF:NMP
100:0	100:0	100:0	100:0	100:0	100:0
90:10					
80:20	80:20	80:20	80:20	80:20	80:20
70:30					
60:40	60:40	60:40	60:40	60:40	60:40
50:50			50:50		
40:60	40:60	40:60	40:60	40:60	40:60
30:70					
20:80	20:80	20:80	20:80	20:80	20:80
10:90					
0:100	0:100	0:100	0:100	0:100	0:100

- **$MAPbBr_3$ precursor solution.** $MAPbBr_3$ precursor solution was synthesised by mixing stoichiometric amounts of MABr and $PbBr_2$ in 5 mL of DMF to obtain a 0.8 M solution. The solution was stirred at 60 °C under a nitrogen atmosphere for 1 h. Samples for further SAXS measurement were taken after 30 and 60 min by introducing a thin (wall thickness of 0.1 mm) rectangular borosilicate capillary (CM Scientific) into the solution.
- **$MAPbCl_3$ precursor solution.** $MAPbCl_3$ precursor solution was prepared in a 50 mL round bottom flask by mixing stoichiometric amounts of MACl and $PbCl_2$ in 5 mL of DMF:DMSO 50:50 to obtain a 0.8 M solution. The solution was stirred at 60 °C under a nitrogen atmosphere for 1 h. Samples for further SAXS measurement were taken after 30 and 60 min by introducing a thin (wall thickness of 0.1 mm) rectangular borosilicate capillary (CM Scientific) into the solution.
- **$FAPbI_3$ precursor solutions.** Formamidinium lead triodide precursor solution was prepared by mixing the precursors (FAI and PbI_2) with the solvent of choice in a 50 mL round-bottom flask. $FAPbI_3$ precursor solutions were prepared using GBL, GBL:DMF 50:50 and DMF as solvents. The solution was stirred at 60 °C under a nitrogen atmosphere for 1 h. Samples for further SAXS measurement were taken after 30 and 60 min by introducing a thin (wall thickness of 0.1 mm) rectangular borosilicate capillary (CM Scientific) into the solution.
- **$APbI_3$ precursor solutions.** Fully inorganic halide perovskite precursor solutions were investigated, where A = Na, K, Rb and Cs. The solvent used for the preparation of $CsPbI_3$ precursor solution was DMF:DMSO 20:80; the other fully inorganic halide perovskite precursor solutions were synthesised using GBL, GBL:DMF 50:50 and DMF as solvents. The precursor solutions were produced in a 50 mL round bottom flask by mixing the precursors in 5 mL of the solvent of choice to obtain a 0.8 M solution. The solution was stirred at 60 °C under a nitrogen atmosphere for 1 h. Samples for further SAXS measurement were taken after 30 and 60 min by

introducing a thin (wall thickness of 0.1 mm) rectangular borosilicate capillary (CM Scientific) into the solution.

2.2. Analytical techniques

Two types of samples were produced: bulk $MAPbI_3$ (crystalline solid) and halide perovskites with different composition precursor solutions (liquid). The solid samples were investigated with X-ray diffraction (XRD), whereas the liquid samples were analysed with small-angle X-ray scattering (SAXS). Both techniques are explained in detail in the following sections.

2.2.1. X-ray diffraction (XRD)

X-ray diffraction is a non-destructive analytical technique used to investigate the phase composition and structure of crystalline materials. X-rays were discovered by Wilhelm Conrad Röntgen in 1895[23] granting him the first Nobel Prize in Physics[24] in 1901. In 1914, Max von Laue received the Nobel Prize in Physics[24] due to the discovery of X-ray diffraction by crystals[25] which established the foundation for X-ray crystallography. Based on Max von Laue's discovery, William Lawrence Bragg and William Henry Bragg conducted experiments with X-ray diffraction to elucidate the crystal structure of different materials, such as KBr, KCl, KI and zinc blende.[26,27] This marked the beginning of the experimental study of crystal structure, establishing XRD as a powerful technique for studying the crystal structure of materials.

W. L. Bragg and W. H. Bragg formulated a law which describes the relationship between the wavelength of X-rays, the angle of incidence, and the distance between crystal planes that leads to constructive interference (diffraction) (Figure 2.4). This is known as Bragg's law (equation 2.1), for which they received the Nobel Prize in Physics in 1915.[24]

$$n \cdot \lambda = 2 \cdot d_{hkl} \cdot \sin\theta \tag{2.1}$$

Where γ is the wavelength of the incident wave, n is an integer, d_{hkl} is the distance between crystal planes, and θ is the incident wave angle.

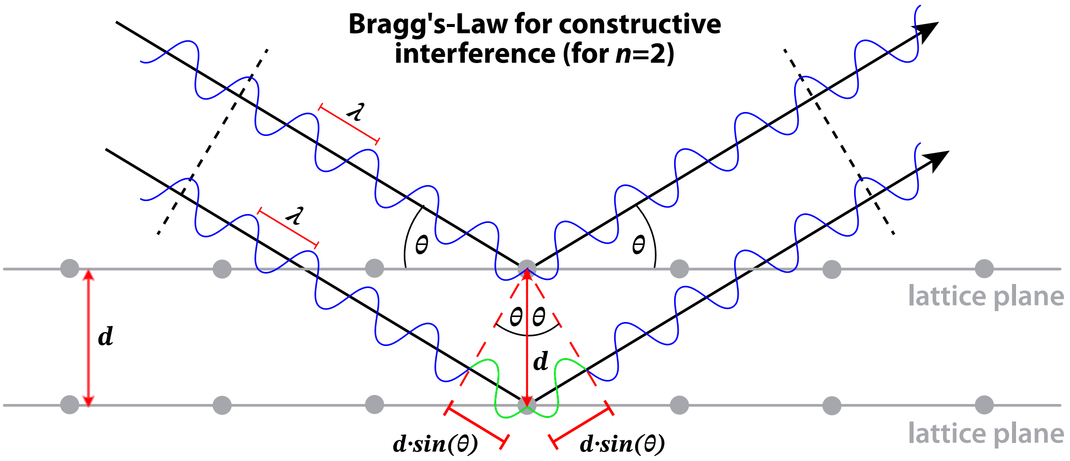

Figure 2.4. Illustration of Bragg's law.[28]

A diffractometer generates X-rays in the X-ray tube containing a cathode and an anode. Typically, a tungsten filament in the cathode is heated by an electric current, emitting electrons into the tube. The electrons are accelerated towards the anode, impacting the target (typically copper or molybdenum). The collision displaces some inner-shell electrons, causing the outer-shell electrons to fall into the lower energy levels to fill the vacancies. The energy loss is emitted as X-rays at a particular wavelength. A Cu target emits Kα ($K\alpha_1 + K\alpha_2$ radiation with a wavelength of 1.54060 and 1.54443 Å, respectively) and K_β radiation with a wavelength of 1.39222 Å. The X-rays are collimated to eliminate unwanted radiation and to produce monochromatic radiation. The filtered X-rays are directed to the powder sample, which is composed of randomly oriented crystallites. Incident X-rays interact with the polycrystalline sample, but only when Bragg's law's conditions are met do they diffract towards the detector. The diffracted X-rays are collected at the detector. The diffraction pattern obtained is characteristic of each material.

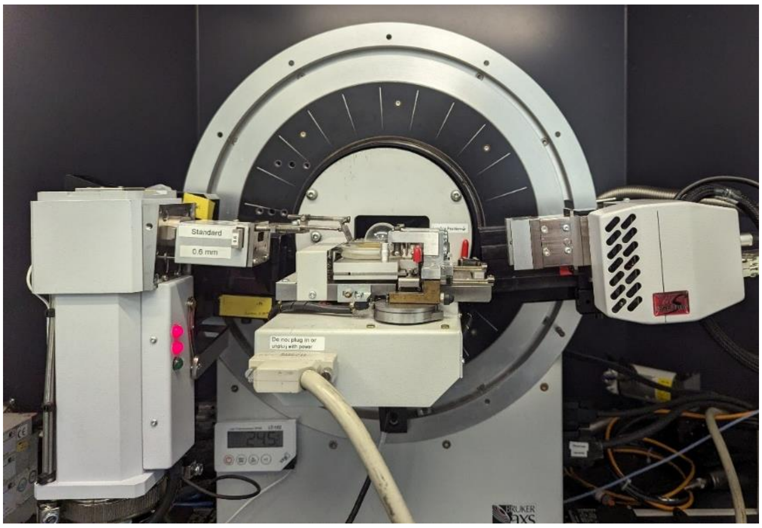

Figure 2.5. Bruker D8 Advance diffractometer under Bragg-Brentano geometry.

- **Le Bail analysis**

The Le Bail method was developed by Armel Le Bail in 1988. It was used for the first time to refine the unit cell parameters of $LiSbWO_6$ without the need for atomic coordinates.[29] It is a whole powder pattern fitting (WPPF) method where the experimentally obtained diffraction pattern is compared to a simulated diffraction pattern without requiring a full structural model, distinguishing it from the Rietveld method.[30] The integrated intensity ($I_k(obs)$) can be calculated with equation 2.2.

$$I_k(obs) = \sum_j \left\{ w_{i,k} S_k^2 \frac{y_i(obs)}{y_i(calc)} \right\} \qquad 2.2$$

Where $w_{i,k}$ is a measure of the contribution of the Bragg peak at position $2\theta_k$ to the diffraction profile y_i at position $2\theta_j$, S_k^2 is the structure factor, and $y_i(obs)$ and $y_i(calc)$ are the observed and calculated diffraction profiles, respectively.

The initial step of a Le Bail analysis is to give an initial value of S_k^2 to obtain $I_k(obs)$. Then, the obtained value is reintroduced as S_k^2 at the next iteration while the cell parameters are refined by least squares. This process allows the determination of the unit-cell parameters, the peak shape parameters, the peak width parameters, and the instrumental shift.

In this dissertation, the following parameters were refined:

- Instrument-related parameters such as zero-shift and asymmetry parameters
- Background
- Lattice parameters $a, b, c, \alpha, \beta, \gamma$
- Caglioti[31] peak-profile parameters U, V and W
- Strain and size parameters: X, Y

The XRD diffraction patterns were measured using a Bruker D8 Advance diffractometer with Cu $K_{\alpha 1}$ and Cu $K_{\alpha 2}$ radiation (λ = 1.54060 Å and 1.54443 Å, respectively). The 2θ angle was measured in the range of 10° and 140° with a step width of 0.02° and a time per step of 1.3 s. A total of 4054 steps were taken. LaB_6 served as the internal standard with a certified lattice parameter of 4.156832(8) Å at 22.5 °C. All measurements were conducted at room temperature and were collected by a LynxEye detector. The phase purity was confirmed by comparing the experimental data with a simulated diffraction pattern using the PowderCell[32] software. Additionally, Le Bail refinement was performed using FullProf Suite.[33] The simulated phases were downloaded from the Inorganic Crystal Structure Data Base (ICSD).[34]

2.2.2. Small angle X-ray scattering (SAXS)

2.2.2.1. Basic principle of SAXS

Small angle X-ray scattering (SAXS) is a powerful, non-destructive technique based on the scattering length density difference between the scattering objects and their surroundings (matrix) between 0.5 – 100 nm. With SAXS, it is possible to determine the size and shape of the scattering objects (form factor) as well as the average distance and the interaction between the scattering objects (structure factor).

The X-rays produced by the source pass through the collimation system to eliminate unwanted wavelengths and to narrow the beam. The incoming X-rays ($\overrightarrow{k_i}$) are scattered by the atoms in the sample, producing coherent scattering (note that incoherent scattering is also produced, but it is negligible at small angles) ($\overrightarrow{k_s}$) which is collected at the detector (Figure 2.6). X-rays interact with the electron cloud of the atoms; therefore, atoms with high atomic numbers scatter more than light atoms.[35,36] The scattering patterns obtained from the measurement are presented as a function of q, which is the length of the scattering vector.

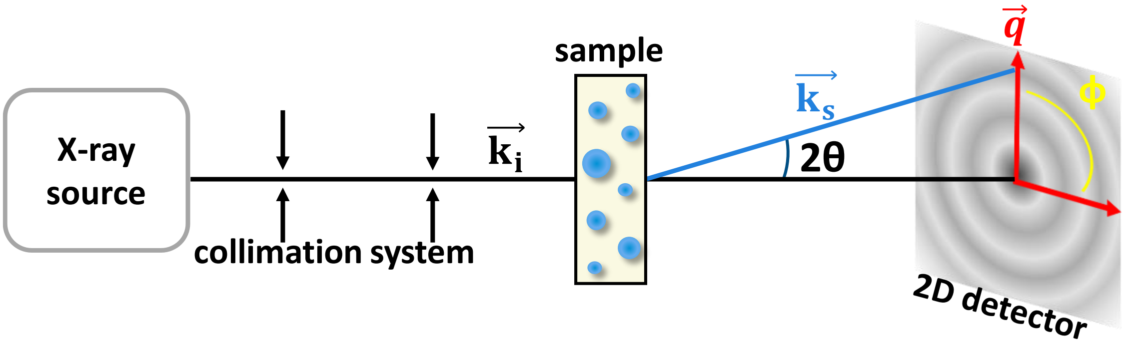

Figure 2.6. Scheme of a SAXS instrument.

$$|\vec{q}| = \frac{4\pi \sin\theta}{\lambda} \quad 2.3$$

SAXS is a very versatile technique which can be applied to an extensive range of topics, such as food science,[37] proteins,[38] liquid crystals,[39] batteries,[40] catalysis,[41–43] and perovskite PV.[44,45]

2.2.2.2. Interpretation of SAXS data: peak position and integral intensity

The detector collects the 2D image (Figure 2.7a) and, after data reduction, it is transformed into a 1D scattering pattern (Figure 2.7b).

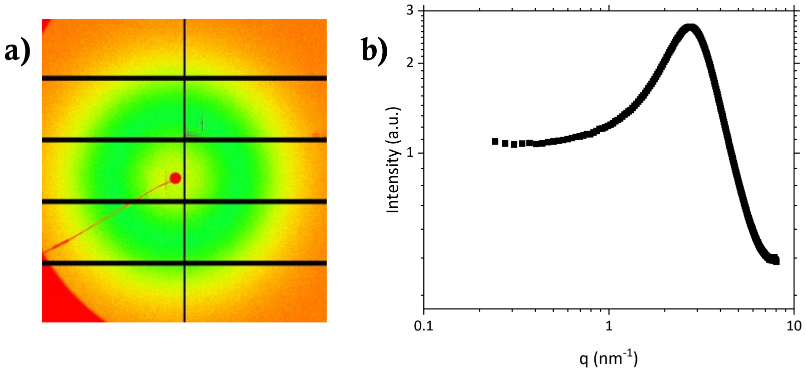

Figure 2.7. a) Detector image after a SAXS measurement. b) Example of a SAXS pattern, S(q) ≠ 1.

The intensity ($I(q)$) in the SAXS pattern can be described using the equation 2.4,

$$I(q) = N_p \int \{\Delta\rho \cdot V_p(r) \cdot P(q)\}^2 \cdot S(q) \cdot N(r) dr + B \qquad 2.4$$

Where:

- N_p is the number of particles
- $\Delta\rho$ is the difference in the scattering length density between the scattering objects and the matrix
- $V_p(r)$ is the volume of one particle
- $P(q)$ is the form factor
- $S(q)$ is the structure factor, $S(q) = 1$ when the sample is diluted.
- $N(r)$ is the size distribution
- B is the background

The data obtained from the SAXS measurements can be analysed using two approaches: model-free analysis or a fit with a model function. Model-free analysis is only possible when the sample is diluted so the scattering objects do not interact with each other. In that case, the structure factor is negligible. Typically, there are three regions in a SAXS pattern: the Guinier, intermediate, and Porod regions. The Guinier region occurs at low-q values and gives information about the size of the scattering objects, which can be obtained from the radius of gyration (R_G). The radius of gyration is the average squared distance of the scatterers from the centre of the object, it can be obtained with the Guinier law[46] (equation 2.5) after plotting $\ln\big(I(q)\big)\ vs\ q^2$.

$$I(q) = I_0 \cdot e^{\left(-\frac{q^2 \cdot R_G^2}{3}\right)} \qquad 2.5$$

The intermediate region gives information about size distribution, and the Porod region provides information about the surface area. In this region, the slope of the pattern is approximately q^{-4}. Not all regions must be present in a SAXS pattern.

In the other approach, the fit with a model, the experimental scattering pattern is compared with calculated models to obtain the form and structure factors. The form factor contains information about the size and shape of the scattering objects, whereas the structure factor describes their interaction.[35,36,47] The scattering objects can be monodisperse (all particles have the same size) or polydisperse (the size of the particles is described by a size distribution) (Figure 2.8a, Figure 2.8b). As an example, the form factor for monodisperse spherical particles, considering a dilute solution, is shown in equation 2.6, where r is the radius of the particle, $\Delta\rho$ is the scattering length density difference, and q is the length of the scattering vector. A lognormal size distribution was used to describe the size of polydisperse samples (equation 2.7), where A is the scale factor, p is the shape parameter, σ is the width parameter (polydispersity), μ is the location parameter (median of the size distribution when $p = 1$) and r_i are the radii of the particles. The form factor of a sphere was used for the data analysis in all samples.

$$P(q) = \frac{4}{3}\pi r^3 \cdot \Delta\rho \cdot 3 \cdot \frac{\sin(qr) - qr \cdot \cos(qr)}{(qr)^3} \qquad 2.6$$

$$N(r_i) = A \cdot r_i^{-p} \cdot \exp\left(-\frac{\ln\left(\frac{r_i}{\mu}\right)^2}{2\sigma^2}\right) \qquad 2.7$$

When the sample is not diluted, i.e. the particles interact with each other, the structure factor $S(q)$ must be considered. The structure factor provides the interaction between the scattering objects as well as the average distance between the scattering objects (d). The presence of a peak in the scattering object (Figure 2.8d) is an indication of particle interaction. The distance between the scattering objects is calculated with equation 2.8, where q_{max} is the q-value at the peak maximum in the scattering pattern. In this work, the peak position of the SAXS patterns was obtained using a PseudoVoigt1 fit.

$$d = \frac{2\pi}{q_{max}} \tag{2.8}$$

There are several structure factors, depending on the nature of the sample, however this work focuses on the hard sphere model following the monodisperse Percus-Yevick approximation.[48,49] In the hard sphere model, it is considered that the scattering factors cannot be compressed, and they cannot penetrate each other. The structure factor can be described as a function of the radius of the hard sphere (R_{HS}) and the volume fraction of the spheres (f_p), being R_{HS} the minimum possible distance between the scattering objects and f_p the measure of interacting scattering objects in the solution. The hard sphere model is described by equations 2.9 – 2.14.

$$S(q, R_{HS}, f_p) = \frac{1}{1 + 24 \cdot f_p \cdot \frac{G(f_{p,A})}{A}} \tag{2.9}$$

$$\begin{aligned} G(f_p, \mathrm{A}) = {} & \alpha \frac{\sin(A) - A \cdot \cos(A)}{A^2} + \beta \frac{2 \cdot A \cdot \sin(A) + (2 - A^2)\cos(A) - 2}{A^3} \\ & + \gamma \frac{-A^4 \cdot \cos(A) + 4 \cdot [(3 \cdot A^2 - 6)\cos(A) + (A^3 - 6 \cdot A)\sin(A) + 6]}{A^5} \end{aligned} \tag{2.10}$$

$$A = 2 \cdot R_{HS} \cdot q \tag{2.11}$$

$$\beta = -6 \cdot f_p \frac{\left(1 + f_p/2\right)^2}{\left(1 - f_p\right)^4} \tag{2.12}$$

$$\alpha = \frac{(1 + 2 \cdot f_p)^2}{\left(1 - f_p\right)^4} \tag{2.13}$$

$$\gamma = \frac{f_p \cdot \alpha}{2} \tag{2.14}$$

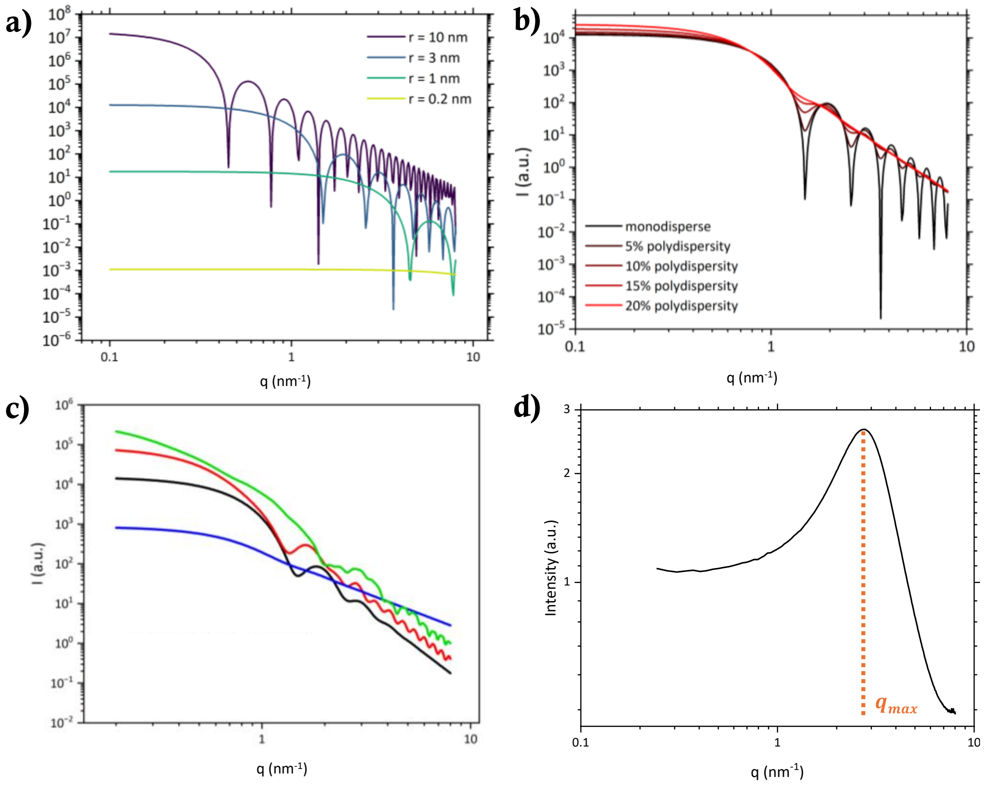

Figure 2.8. a) form factor of particles with different radii. b) form factor of a particle with r = 3 nm showing different polydispersity. c) form factors of parallelepiped (green), disc (blue), cylinder (red) and sphere (black). The radii are 3 nm, and polydispersity is 10%.

All the precursor solutions were measured at Helmholtz-Zentrum Berlin's synchrotron radiation source BESSY II at the four-crystal monochromator beamline[50] in the laboratory of the Physikalisch-Technische Bundesanstalt using the HZB ASAXS instrument[51] at room temperature. The SAXS patterns were recorded using a windowless DECTRIS 1M PILATUS2 in-vacuum hybrid pixel detector.[52] The measurements were taken at 10 keV with a distance between the sample and the detector of 0.8 m, covering a q-range from 0.2 to 8 nm^{-1} (size range: 31.41 – 0.79 nm). Each sample was measured twice at three different points along the capillary for 3 minutes, resulting in an 18-minute total exposure per sample. The 2D scattering images were azimuthally averaged and corrected for instrumental background and contributions of the sample holder with the BerSAS software,[53] the data reduction was done by Dr Armin Hoell, Dr Uwe Keiderling and Niyaz Huseyn-Zada. The resulting 1D scattering curves were analysed using the software SASfit.[54]

Chapter 3. Comparison of $MAPbI_3$ synthesised from solution by different methods

To determine whether the synthesis method has an impact on the structure of $MAPbI_3$, XRD was applied immediately after synthesis. Three synthesis methods were used, the antisolvent method, which takes place at room temperature; the acetate method, which takes place at 40 °C (below the cubic → tetragonal phase transition at 56.85 °C); and the ITC method, which takes place up to 100 °C (above the cubic → tetragonal phase transition).

3.1. Antisolvent method

$MAPbI_3$ crystals were grown using the antisolvent method at room temperature, as described by Rakita et al.[21] This method is based on the diffusion of a solvent within the $MAPbI_3$ precursor solution. The solvent is known as antisolvent since it triggers the precipitation of $MAPbI_3$ due to its low solubility. This method can be used to grow single crystals[55] as well as thin films.[56] This method is characterised by taking place at room temperature and using acetonitrile as the solvent, which is neither harmful to humans nor the environment.[57]

The vials containing the $MAPbI_3$ precursor solution were submerged in ethyl acetate for 14 days to allow the crystals to grow (Figure 3.1). During the first 48 hours, PbI_2 was observed at the bottom of the vials; the first evidence of crystal growth followed this phenomenon.

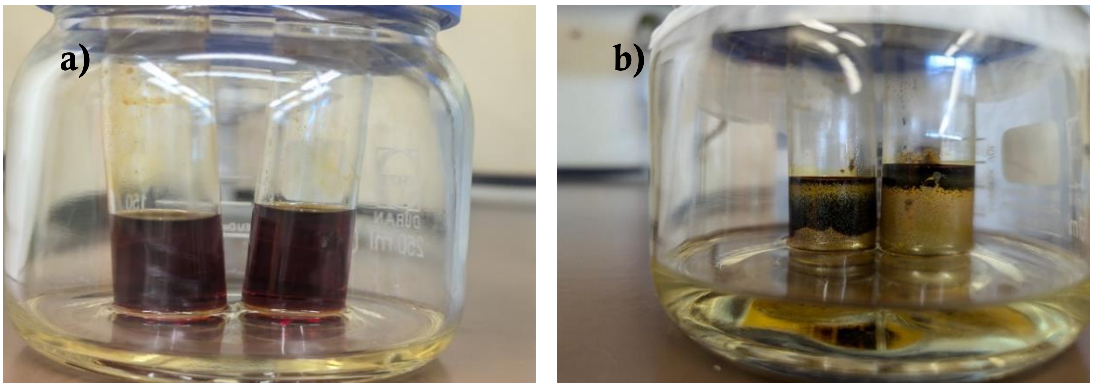

Figure 3.1. a) $MAPbI_3$ precursor solution on day 1. b) $MAPbI_3$ precursor solution after 14 days.

The crystals were allowed to grow for 14 days to ensure enough quantity for an XRD analysis. After that time, the crystals were retrieved from the vials, although covered in PbI_2 (Figure 3.2).

Figure 3.2. $MAPbI_3$ crystals obtained using the antisolvent method, the crystals were covered by PbI_2.

The experimentally obtained diffractogram was compared to $MAPbI_3$ and PbI_2 simulated patterns using the PowderCell software, which showed that both phases were present in the sample.

The lattice parameters of $MAPbI_3$ and PbI_2 were obtained by applying Le Bail analysis to the experimentally obtained diffractogram (Figure 3.3); the fits were performed using the space group $I4cm$ for $MAPbI_3$ obtaining the lattice parameters a = b = 8.871(1) Å and c = 12.669(1) Å. The space group $P\bar{3}m1$ was applied to PbI_2, obtaining the lattice parameters a = b = 4.557(1) Å and c = 6.984(1) Å.

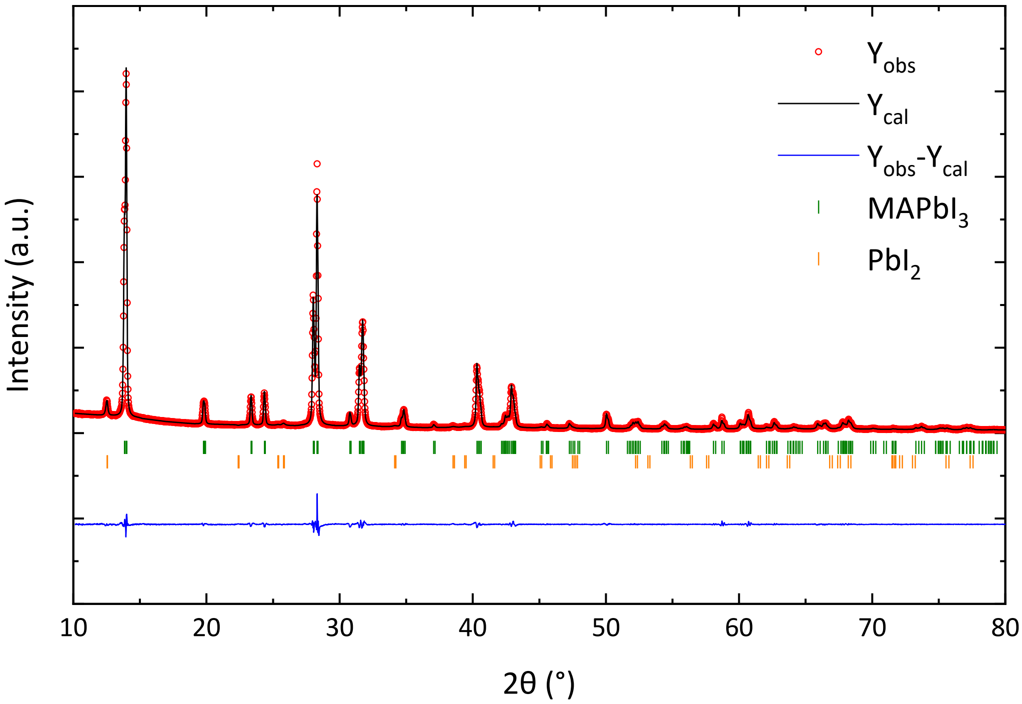

Figure 3.3. Le Bail refinement (black line) of $MAPbI_3$ powder diffraction pattern (red dots) synthesised with the antisolvent method. The difference between the observed and the calculated intensity is shown in blue. $MAPbI_3$ Bragg peaks are shown in green and PbI_2 Bragg peaks are shown in orange.

3.2. Acetate method

$MAPbI_3$ was synthesised using the method presented by Dang et al.,[20] where the source of Pb^{2+} is $Pb(CH_3COO)_2{\cdot}3H_2O$ instead of the commonly used PbI_2. The solvent used in this synthesis was aqueous HI, which also acts as the iodide source to form $MAPbI_3$. This synthesis was conducted at 40 °C, below the cubic → tetragonal phase transition at 56.85 °C.

After the precursors were dissolved, $MAPbI_3$ precursor solution was left undisturbed for 14 days at 40 °C to allow the crystals to grow. During that time, the precursor solution turned from light brown to brown (Figure 3.4a, b) but no crystal growth was observed. Bulk $MAPbI_3$ was formed after solvent evaporation (Figure 3.4c) followed by XRD analysis of the synthesised sample.

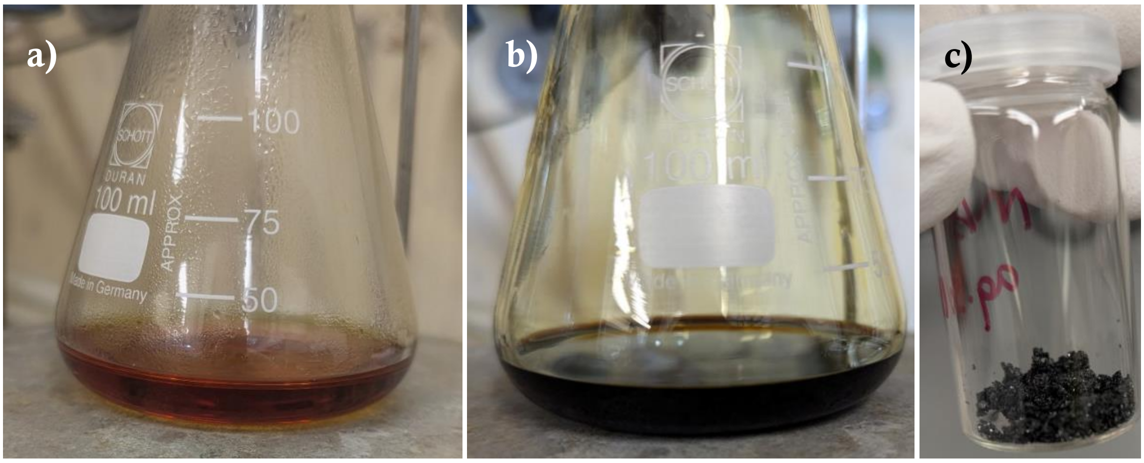

Figure 3.4. a) $MAPbI_3$ precursor solution freshly synthesised. b) $MAPbI_3$ precursor solution after 14 days. c) bulk $MAPbI_3$ obtained with the acetate method.

The experimentally obtained XRD diffractogram was compared with the $MAPbI_3$ and PbI_2 simulated diffraction patterns using the PowderCell software. Le Bail analysis (Figure 3.5) was applied to the diffractogram to obtain the lattice parameters of $MAPbI_3$ and PbI_2. The fits were performed using the space group $I4cm$ for $MAPbI_3$, obtaining $a = b = 8.872(1)$ Å and $c = 12.671(1)$ Å; and the space group $P\bar{3}m1$ was applied to PbI_2, obtaining $a = b = 4.557(1)$ Å and $c = 6.979(1)$ Å.

$MAPbI_3$ single crystals could not be obtained using the acetate method within 14 days. It is possible that the crystals need more time to be large enough to be visible. Upon solvent evaporation, bulk $MAPbI_3$ was received, although obtaining a phase pure sample was not possible. The sample contained PbI_2 as an impurity.

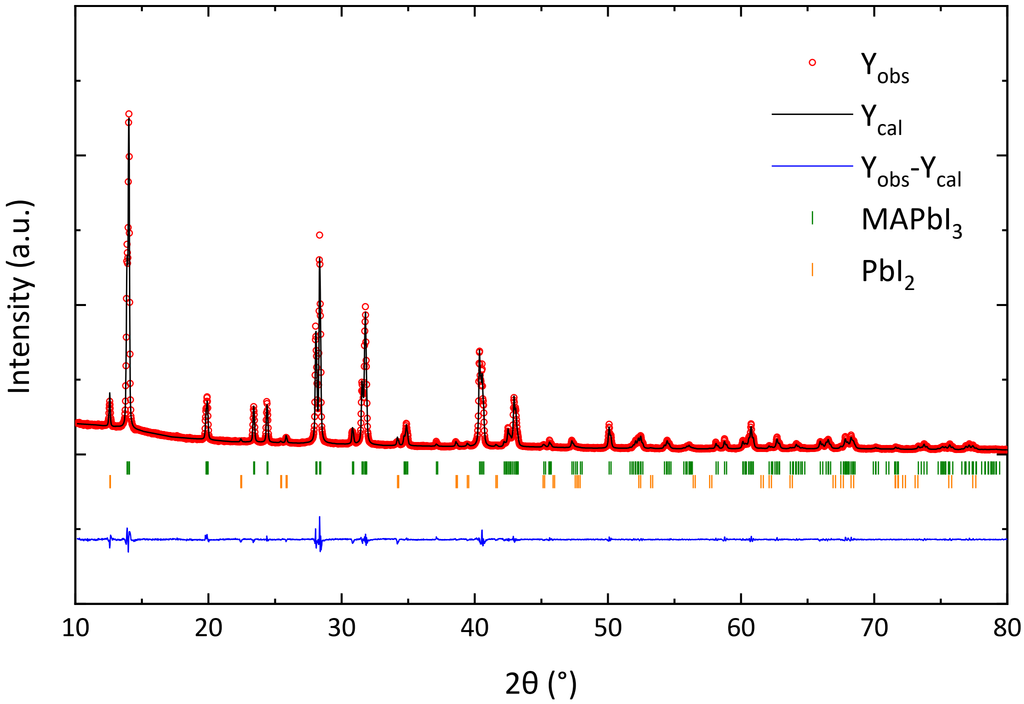

Figure 3.5. Le Bail refinement (black line) of $MAPbI_3$ powder diffraction pattern (red dots) synthesised with the acetate method. The difference between the observed and the calculated intensity is shown in blue. $MAPbI_3$ Bragg peaks are shown in green and PbI_2 Bragg peaks are shown in orange.

3.3. Inverse Temperature Crystallisation method

The inverse temperature crystallisation method is based on the decrease in solubility of $MAPbI_3$ at increasing temperatures. This method can be used to grow hybrid halide perovskites single crystals[16] as well as thin films[58] and bulk material.[59] $MAPbI_3$ was prepared by adapting the method used by Baikie et al.[59] A series of 11 samples was prepared with a variation of the GBL:DMF solvent ratio (Table 2.1).

$MAPbI_3$ powder samples (Figure 3.6) were analysed with XRD immediately after synthesis to verify the phase purity. The experimentally obtained XRD diffractograms were compared with simulated diffraction patterns using the PowderCell software. Most of the synthesised samples were phase pure, except for $MAPbI_3$ prepared with GBL:DMF ratio 10:90 and 0:100. Both samples show a Bragg peak at 12.70° indicating the presence of PbI_2 however, other PbI_2 characteristic peaks do not appear in the diffractogram. Other Bragg peaks which do not correspond to $MAPbI_3$, LaB_6 or PbI_2 were identified at 13.09, 22.63 and 26.31°. These Bragg peaks can be explained by the presence of the intermediate $(MA)_2(DMF)_2Pb_3I_8$.

DMF is a coordinating solvent that bonds to Pb^{2+}, forming Lewis adducts.[60] The crystallisation of $MAPbI_3$ from solution is not a one-step process, it takes place through Lewis adducts intermediates.[61,62] Petrov et al.[63] identified the intermediates involved in the crystallisation of $MAPbI_3$ when DMF is used as the solvent. The intermediates' composition changes with different MAI:PbI_2 ratio, the presence of $(MA)_2(DMF)_2Pb_3I_8$ indicates an excess of PbI_2 in the sample.

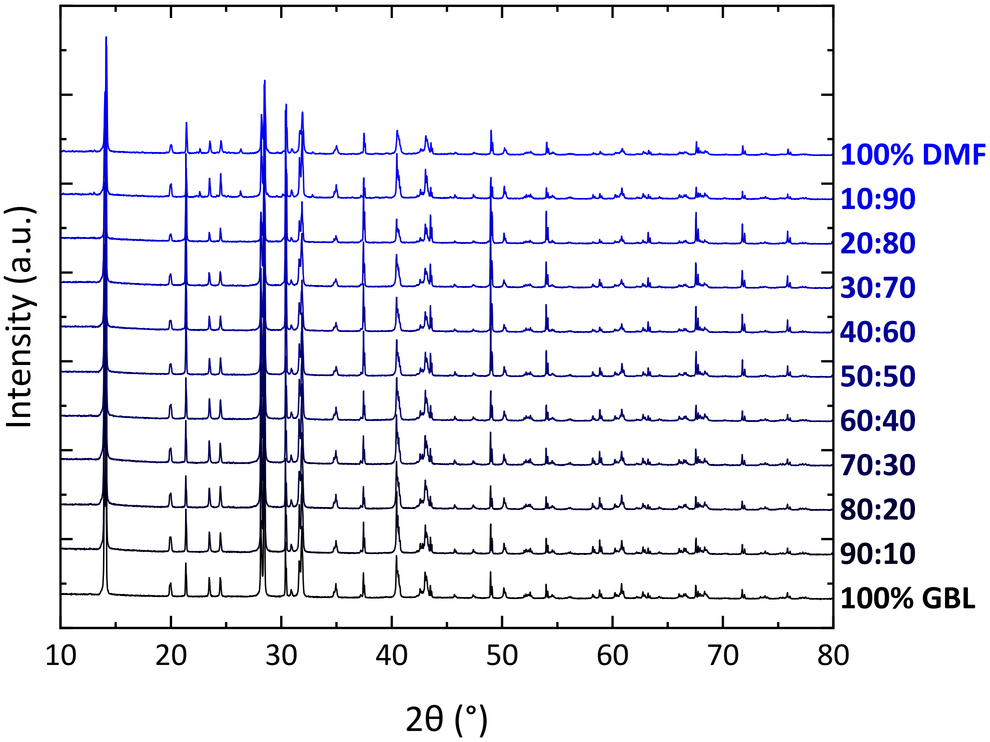

Figure 3.6. Powder XRD patterns of $MAPbI_3$ synthesised with different GBL:DMF solvent ratios, LaB_6 was used as internal standard.

Le Bail profile fitting was applied to all the synthesised samples in order to obtain the lattice parameters (Figure 3.7). The fits were performed using the space group $I4cm$ for tetragonal $MAPbI_3$ and $Pm\bar{3}m$ for LaB_6.

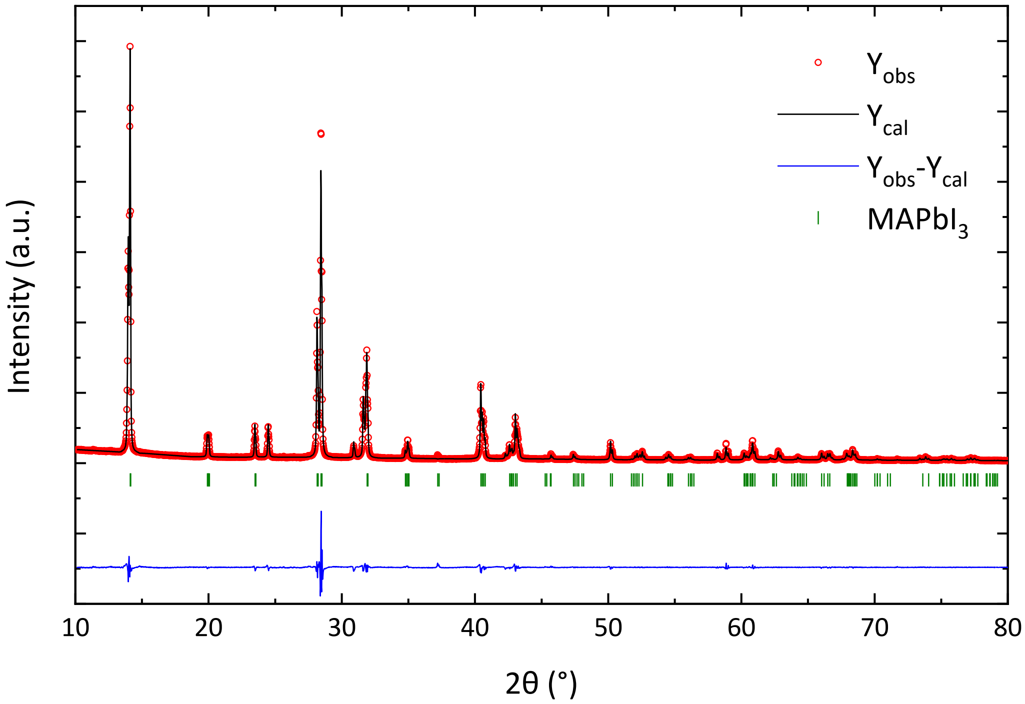

Figure 3.7. Le Bail refinement (black line) of $MAPbI_3$ powder diffraction pattern (red dots) synthesised with the ITC method using GBL as solvent. The difference between the observed and the calculated intensity is shown in blue. $MAPbI_3$ Bragg peaks are shown in green.

The lattice parameters obtained from the Le Bail analysis (Figure 3.8) show slight disparities among the different samples, albeit without a clear trend. Thus, it can be concluded that despite the effect of the solvent in the crystallisation path, the choice of solvent to synthesise $MAPbI_3$ does not have an impact on its crystal structure.

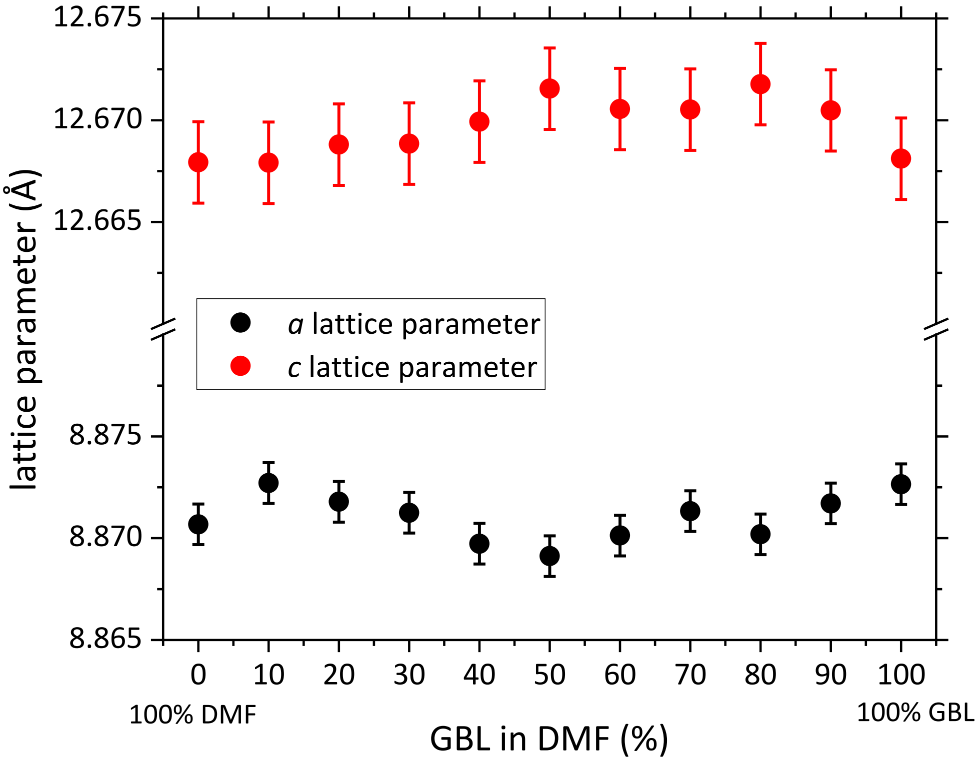

Figure 3.8. Lattice parameters of $MAPbI_3$ synthesised with different GBL:DMF solvent ratios.

3.4. Conclusions

The crystallisation of $MAPbI_3$ was carried out at three different temperatures: at room temperature, at 40 °C and at 100 °C, the latter being above the cubic → tetragonal phase transition at 56.85 °C.

Although $MAPbI_3$ was successfully synthesised with all three methods, only the ITC method was able to deliver phase pure $MAPbI_3$. A series of 11 samples was synthesised with ITC using different GBL:DMF solvent ratios to investigate whether the solvent has an impact on the structure of hybrid halide perovskites. The results obtained from Le Bail refinement of the experimentally obtained diffraction patterns indicate that the lattice parameters do not present significant differences among the samples. Comparing the lattice parameters obtained from ITC with the ones obtained from the antisolvent and the acetate method (Table 3.1), it can be concluded that there are no significant differences between the three methods. Not only does the solvent not influence the structure of the final $MAPbI_3$, but the temperature at which $MAPbI_3$ is synthesised does not play a significant role. Moreover, the presence of PbI_2 as an impurity does not affect the final crystal structure.

Table 3.1. Overview of the solution-based $MAPbI_3$ synthesis methods, the synthesis temperature and the lattice parameters obtained with Le Bail refinement.

$MAPbI_3$ synthesis method	**Temperature (°C)**	**lattice parameter *a* (Å)**	**lattice parameter *c* (Å)**
antisolvent	room temperature	8.871(1)	12.669(2)
acetate	40	8.872(1)	12.671(2)
ITC (GBL)	100	8.873(1)	12.667(2)

ITC is the method of choice for synthesising halide perovskites precursor solutions since it has been proven to produce phase pure $MAPbI_3$ rapidly, with a total synthesis time of 2 hours. On the other hand, the antisolvent method took several days to produce $MAPbI_3$ single crystals; however, a large amount of PbI_2 also precipitated coating all the crystals. Finally, the acetate method did not yield single crystals within 14 days. $MAPbI_3$ crystallised after the evaporation of the solvent, producing a polycrystalline sample. Furthermore, it was not possible to obtain phase pure $MAPbI_3$ with this method.

Chapter 4. Influence of the solvent in the early stage of crystallisation of hybrid halide perovskites: the exemplary case of $MAPbI_3$

This chapter discusses the influence of the solvent in the early-stage crystallisation process of $MAPbI_3$ precursor solutions. To understand the effect of the solvent, four different solvents were investigated: γ-butyrolactone (GBL), N,N-dimethylformamide (DMF), N-methylpyrrolidone (NMP) and dimethyl sulfoxide (DMSO).

4.1. Choice of the solvents and their combinations

One of the characteristics of HHPs is the possibility of being processed from solution. It has been shown that the choice of the solvent not only affects the crystallisation path of HHPs,[61,64] but also the power conversion efficiency of the solar cell.[65] Therefore, understanding the formation mechanism of HHPs in the solution is crucial for controlling the crystallisation process and ultimately improving the performance of a device produced from solution processing. It has been reported in the literature the existence of highly valent iodoplumbates in HHPs precursor solutions[66] as well as the possibility of achieving a power conversion efficiency of 20% by using solvent engineering[67] showing how important it is to understand the solvation chemistry in HHPs precursor solutions. This study aims to gain a deeper understanding of how the solvent interacts with the precursors at the early stage of crystallisation of hybrid halide perovskites. $MAPbI_3$ was chosen as the exemplary compound, although this study can be extended to other compositions (see Chapter 5 and Chapter 6). The solvents selected for this study are GBL, DMF, NMP and DMSO and mixtures (Figure 4.1a), which are typically used for the synthesis of single crystals[68] as well as thin films.[69,70]

Gutmann's donor number (DN) is a scale used to measure the electron-donating ability of solvents. This is defined as the negative enthalpy ($-\Delta H$ in kcal/mol) for the interaction of the electron pair of the solvent with $SbCl_5$ in a highly diluted dichloroethane solution.[71] Applied to the HHPs field, DN determines a solvent's ability to solvate species in the precursor solution (Figure 4.1b).

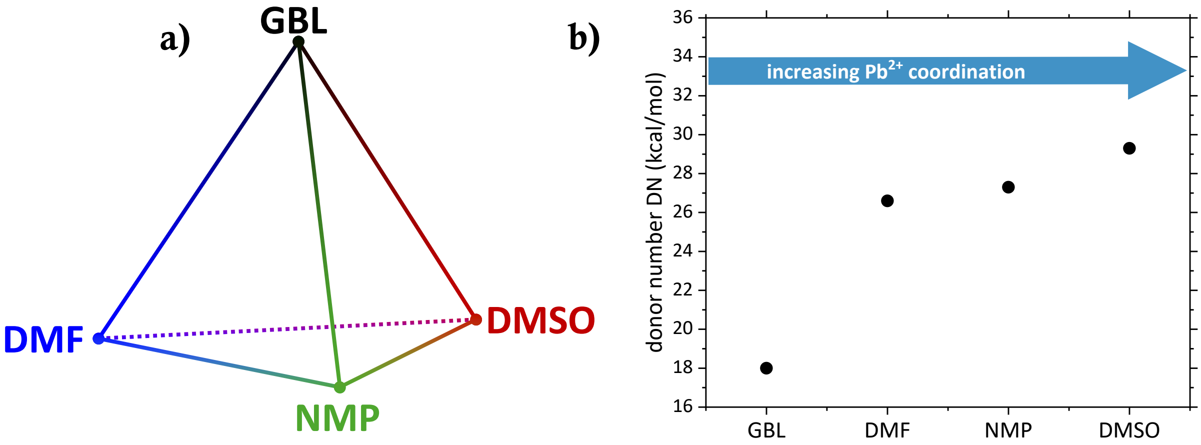

Figure 4.1. a) Solvents and solvent mixtures studied. b) Donor number of the solvents used in this study.[72]

Solvents with high DN, such as DMSO, compete with I^- to coordinate with Pb^{2+}. This results in the formation of intermediates,[73] which leads to a decrease in the number of iodoplumbates in the solution due to the lower Pb^{2+} availability.[74] This makes DMSO, or solvents with high DN in general, ideal for thin film processing. On the other hand, solvents with low DN, such as GBL, which do not have such coordinating capacity, are more suitable for HHPs single crystal growth.

4.2. Interaction of scattering objects in the solution

The synthesised $MAPbI_3$ precursor solutions in different solvents (Table 2.1) were analysed with SAXS to determine the morphology (form factor) as well as the interaction (structure factor) between the scattering objects. The SAXS patterns of all the measured samples show a peak in the scattered intensity at q-values between 2.5 and 3.3 nm^{-1}, demonstrating that the scattering objects in solution agglomerate. From the peak position, it is possible to calculate the average distance between the scattering objects (experimental distance, d_{exp}). The experimental distance was calculated for all the $MAPbI_3$ solvent series (Figure 4.2), showing that there is a correlation between the average distance between the scattering objects and the solvent fraction.

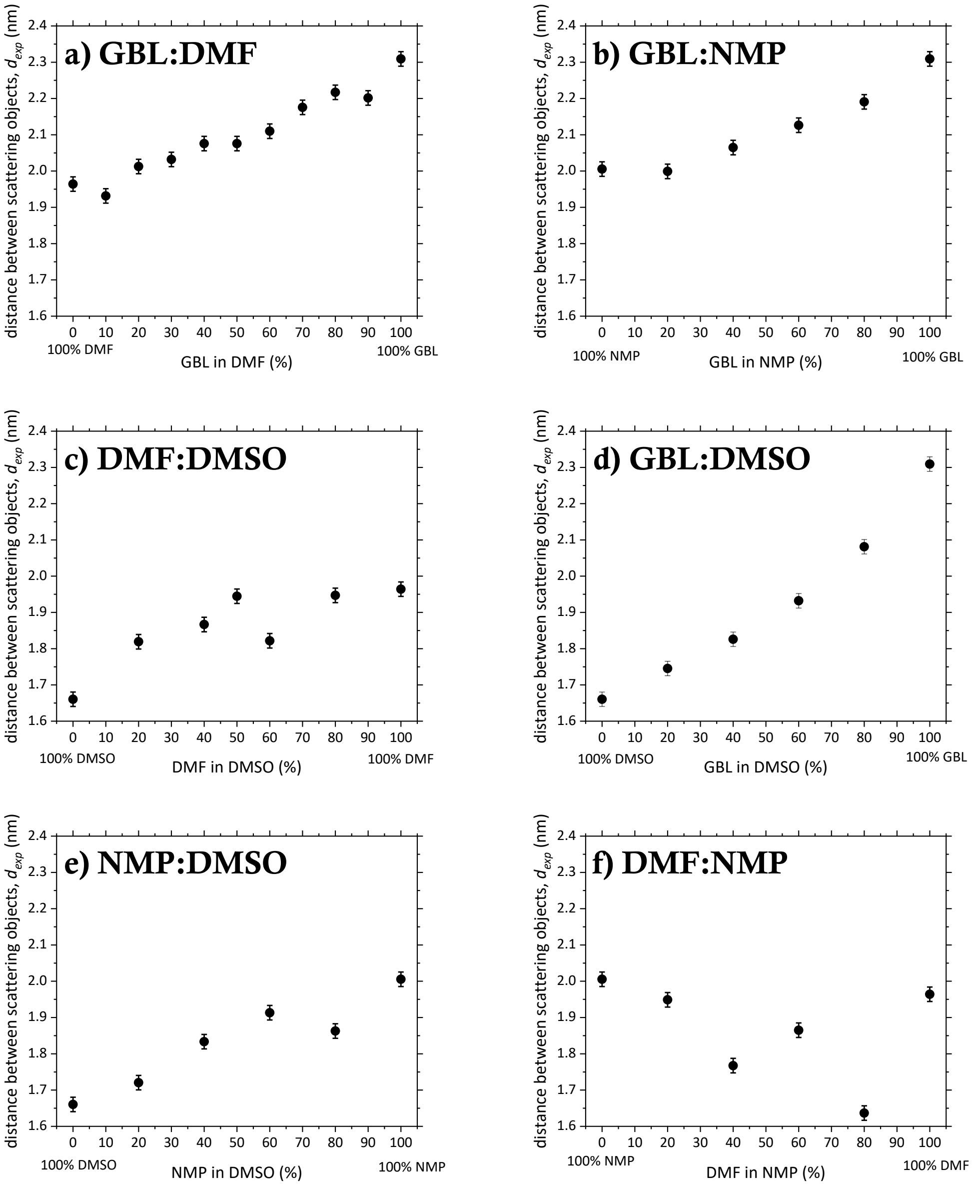

Figure 4.2. Distance between scattering objects in $MAPbI_3$ precursor solution synthesised with different a) GBL:DMF, b) GBL:NMP, c) DMF:DMSO, d) GBL:DMSO, e) NMP:DMSO and f) DMF:NMP solvent ratios.

To understand what is the origin of the difference in d_{exp} within the same binary mixture, the size of the solvent molecules was calculated with DFT. The DFT calculations were performed completely by Prof. Joachim Breternitz, which are explained elsewhere.[75] The molecules were modelled as ellipsoids, which are defined by 3 radii. It is considered that the solvent molecules are randomly oriented, for this reason, the geometrical mean ($\bar{r}_s$) was used for the calculations (Table 4.1, equation 4.1, Figure 4.3)

$$\bar{r}_s = \sqrt[3]{r_{s1} r_{s2} r_{s3}} \tag{4.1}$$

The size difference between the end members solvent molecules cannot explain the difference in d_{exp} between the scattering objects.

Table 4.1. Radii of GBL, DMF, NMP and DMSO calculated with DFT.[76]

solvent	r_{s1} **(nm)**	r_{s2} **(nm)**	r_{s3} **(nm)**	$\bar{r}_s$ **(nm)**
GBL	0.188	0.211	0.314	0.232
DMF	0.150	0.245	0.306	0.224
NMP	0.192	0.278	0.325	0.259
DMSO	0.168	0.240	0.261	0.219

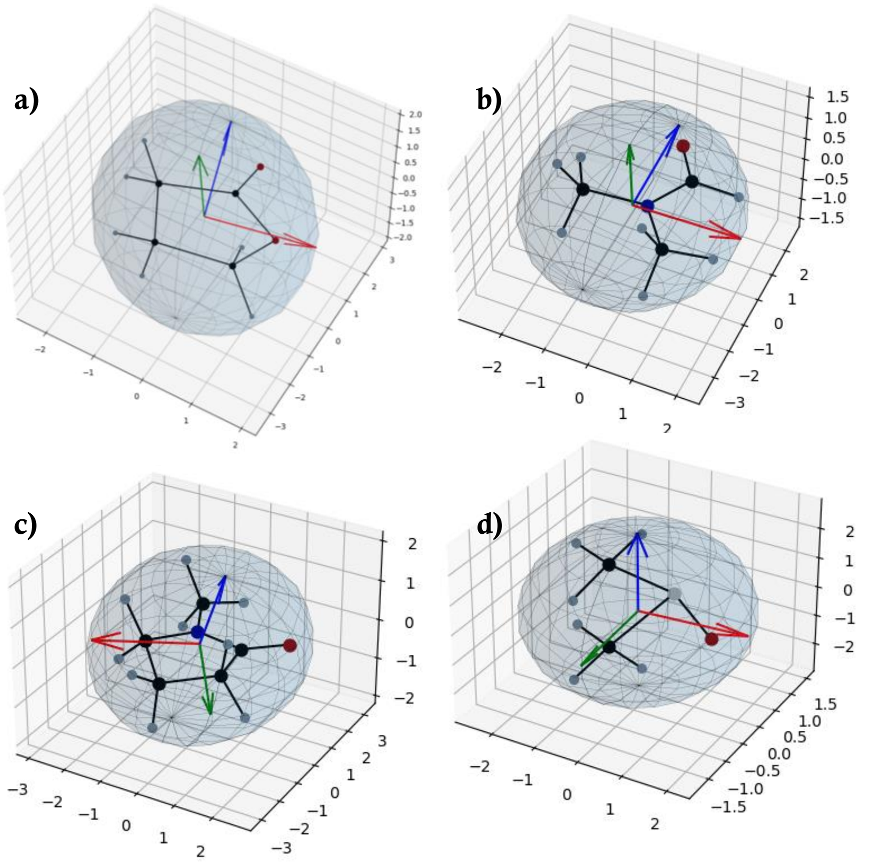

Figure 4.3. Solvent molecules modelled as ellipsoids, a) GBL, b) DMF, C) NMP, d) DMSO. In all figures, the green arrow represents the shortest radius, the red arrow the medium radius and the blue arrow corresponds to the largest radius.[76]

These results confirm that the solvent is not just the media where the precursors are dissolved, but it plays an important role in HHPs early stage of crystallisation. All the solvent series show differences in d_{exp} within the same binary mixture; furthermore, not all the solvent series follow the same trend. Comparing the d_{exp} value for the end members with their donor numbers (Figure 4.4), it is clear that there is a correlation between them. As expected, high DN results in lower d_{exp} due to the interaction of the solvent with Pb^{2+}, preventing the formation of large iodoplumbates.

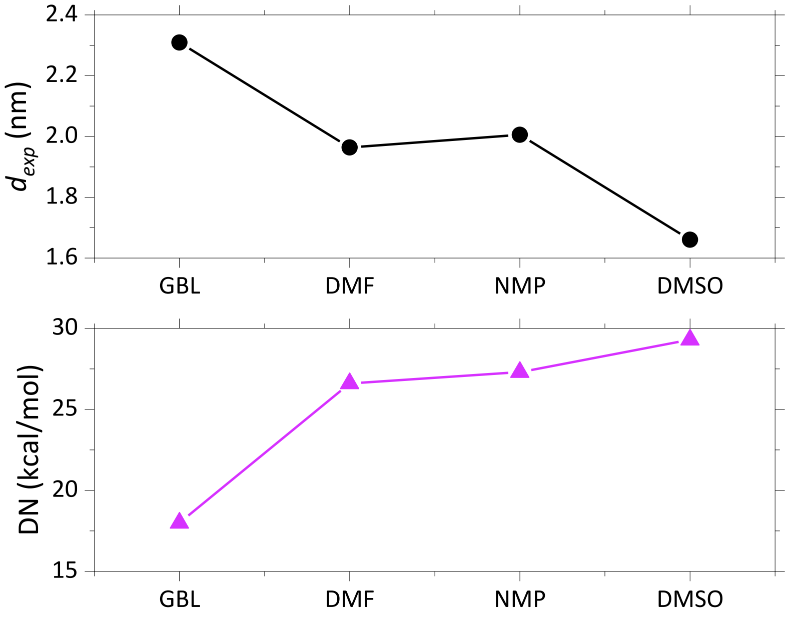

Figure 4.4. Comparison between the solvents' DN and their d_{exp}. The error of d_{exp} is smaller than the points.

Based on the information that the size of the agglomerates changes with the solvent and that the change is correlated with the DN, a model that describes the scattering objects present in HHPs precursor solution was developed.

4.3. The development of the core-shell model

It was proven that the solvent must be part of the scattering objects, for this reason, a core-shell model where the core is formed by [PbI_6] octahedra surrounded by solvent molecules was developed (Figure 4.5). This model combines the information obtained by SAXS using different solvents as well as the information from literature[66,77] where the presence of highly valent iodoplumbates in HHPs precursor solutions is reported. For this model, the interaction between Pb^{2+} and the solvent is not considered.

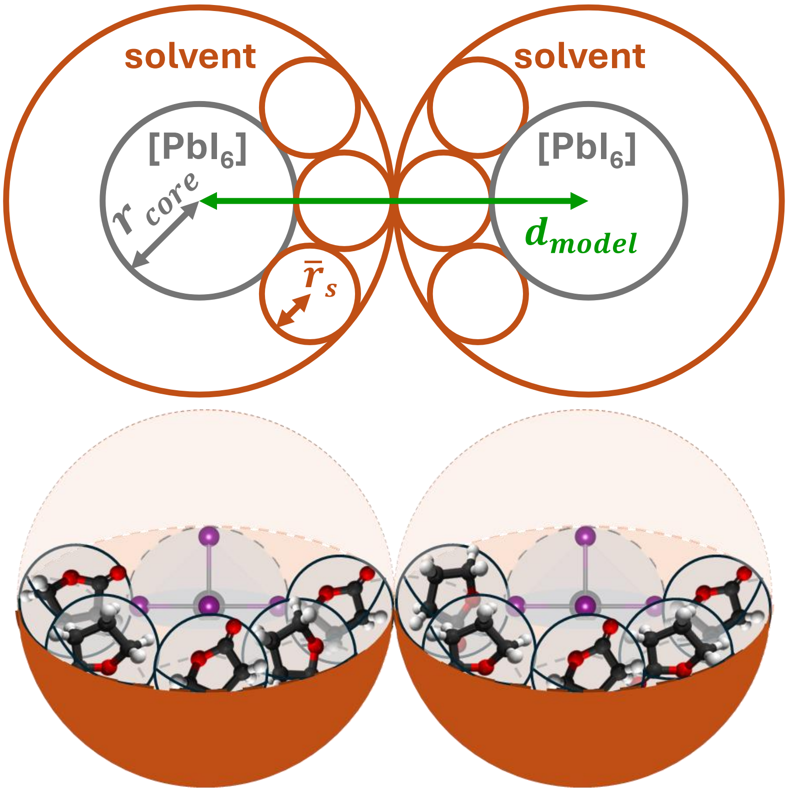

Figure 4.5. a) Scheme of the core-shell model. The [PbI_6] octahedra core, which can be arranged as a single octahedron ($[PbI_6]^{4-}$) or as corner-sharing octahedra ($[Pb_2I_{11}]^{7-}$), is surrounded by randomly oriented solvent molecules. The distance between the centre of mass between the scattering objects is shown as d_{model}. b) Example of the core-shell model showing a $[PbI_6]^{4-}$ octahedron as the core surrounded by randomly oriented GBL molecules.

The core is formed by [PbI_6] octahedra, which can be arranged as a single octahedron $[PbI_6]^{4-}$ or as a corner-sharing octahedra $[Pb_2I_{11}]^{7-}$. When the core is formed by a single octahedron, the radius of the core (r_{core}) can be described as the sum of the Pb-I bond length and the radius of the outer anion (r_{I^-}) (equation 4.2). Whereas when the core is composed of a corner-sharing octahedra, its radius is calculated as the sum of twice the Pb-I bond length and the radius of the outer anion (equation 4.3). The radius of I^-, as well as the Pb-I bond length, were calculated with DFT by Prof. Joachim Breternitz, where the Pb-I bond length is 0.319 nm and the radius of I^- is 0.167 nm. The core is surrounded by randomly oriented solvent molecules; for this reason, the geometric mean of the ellipsoid's radii is used for the calculations (equation 4.1).

$$r_{core}^{single\ octahedra} = Pb - X + r_{X^-} \tag{4.2}$$

$$r_{core}^{corner-sharing} = 2 \cdot (Pb - X) + r_{X^-} \tag{4.3}$$

Considering the I^- radius and the Pb-I bond length, $r_{core}^{single\ octahedra} = 0.484\,nm$ and $r_{core}^{corner-sharing} = 0.803\,nm$. Combining the two core arrangements and the radius of the solvent, it is possible to describe the distance between two adjacent scattering objects as equation 4.4:

$$d_{model} = 2r_{core} + 4\bar{r}_s \tag{4.4}$$

The average distance between scattering objects can be explained by applying the core-shell model. The core can be arranged as a single octahedron or as a corner-sharing octahedra, and it is surrounded by randomly oriented solvent molecules. The equation was applied assuming that $d_{exp} = d_{model}$, in order to determine the proportion of the core arranged as a single octahedron or as corner-sharing octahedra (Figure 4.6). It can be observed that with increasing DN, the single octahedron core fraction also increases, reaching 97 and 100% when DMSO and NMP are used as solvents, respectively. Interestingly, when the equation was applied to d_{exp} obtained from the sample prepared in DMSO, the result was completely unrealistic since the fraction of single octahedron was over 100%. This is because $\bar{r}_s$ is too large. DMSO binds to Pb^{2+} through the atom O, moreover, the shortest bond in the molecule is C=O with a value of 1.471(8) Å.[78,79] Taking that into consideration, the shortest radius was used for the calculation of the core arrangement, obtaining that 97% of the core is arranged as a single octahedra. Since the atoms and molecules are constantly in motion it is most likely that the core fraction of $MAPbI_3$ in DMSO is 100%.

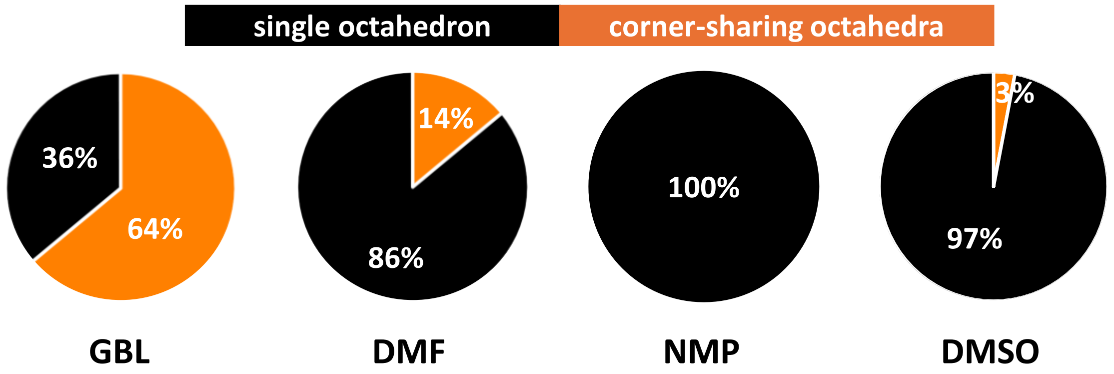

Figure 4.6. Proportion of single octahedra (black) and corner-sharing octahedra (orange) in the core as a function of the solvent.

4.4. The polydispersity in the solvent series

The structural information was obtained by fitting the SAXS patterns using the SASfit software,[54] the data were fitted to a model-based form factor. The shape of the scattering objects was modelled as spheres for all the studied precursor solutions. The analysis of the SAXS data shows that the precursor solutions synthesised with 100% GBL and 100% DMF present polydispersity, whereas the precursor solutions synthesised with 100% NMP and 100% DMSO are monodisperse. These results agree with the model proposed to describe the scattering objects in solution. The median of the polydisperse size distributions was fixed at 0.319 nm, which is the Pb-I bond length. The particle radii obtained for the solutions synthesized with 100% NMP and 100% DMSO were 0.396 and 0.202 nm, respectively. The polydispersity index varies with the solvent fraction (Figure 4.7), comparing the effect of GBL in NMP and GBL in DMF, it can be observed that due to the higher DN of NMP the polydispersity index decreases within the solvent rapidly. This effect is more pronounced when DMSO is used in the solvent mixture.

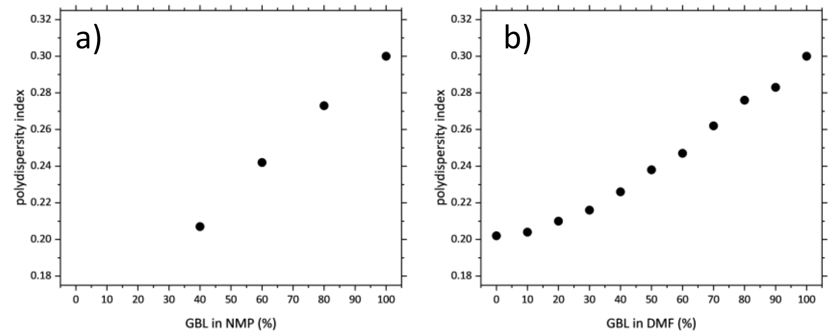

Figure 4.7. Example of polydispersity index of $MAPbI_3$ in precursor solution as a function of the solvent. The precursor solutions were synthesised in GBL:NMP and GBL:DMF.

4.5. The model of the hard sphere radius

The interaction between the scattering objects was modelled as hard spheres. The hard sphere model assumes that the scattering objects cannot be compressed and cannot penetrate each other. The radius of the hard sphere (R_{HS}) is the minimum distance between two adjacent scattering objects (Figure 4.8). R_{HS} was found to be smaller than half of the experimental distance (d_{exp}) for all the solutions, therefore the scattering objects must be able to achieve a smaller arrangement in the core and the shell in order to reach the minimum distance. The smallest possible arrangement in the core is as a single octahedron. Since the solvent molecules were assumed to be randomly oriented for the core-shell model, in order to achieve the minimum distance it is considered that the solvent molecules have a preferred orientation.

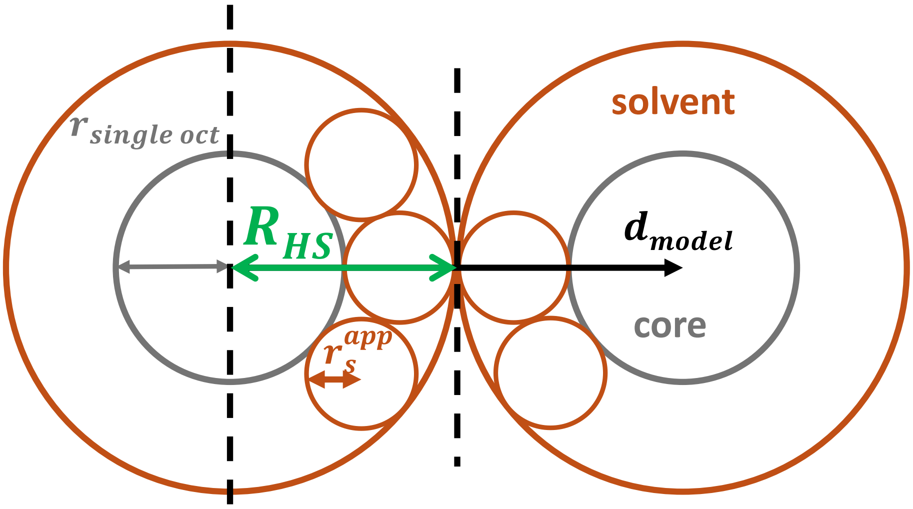

Figure 4.8. Scheme of the radius of the hard sphere (R_{HS}).

The radius of the hard sphere can be defined as (equation 4.5)

$$R_{HS} = r_{core}^{single} + 2r_s^{app} \tag{4.5}$$

where r_{core}^{single} is the radius of the core arranged as a single octahedron and r_s^{app} is the radius of the solvent molecule (apparent radius) to achieve the minimum distance between the scattering objects. The apparent radius calculated for $MAPbI_3$ precursor solution synthesised in GBL:DMF (Figure 4.9) shows that the radius of the solvent always lies within the values of the ellipsoid radii, indicating that the model is consistent.

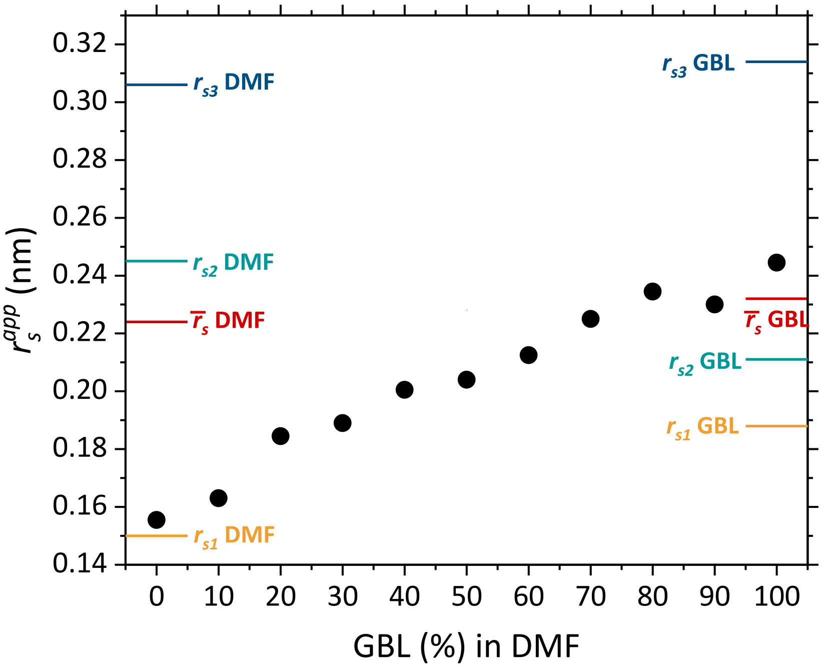

Figure 4.9. Apparent radius for $MAPbI_3$ synthesised in different GBL:DMF solvent ratios.

4.6. Conclusions

$MAPbI_3$ precursor solution was synthesised with solvents commonly used for the synthesis of HHP layers, such as GBL, DMF, NMP, DMSO and mixtures. It was shown that d_{exp} is correlated with Gutmann's donor number, increasing DN in a solvent results in lower d_{exp} between the scattering objects. The experimental distance varies with the solvent ratio, although the variation cannot be explained only by the difference in the size of the solvent molecules. For this reason, a core-shell model was developed. The core is formed by $[PbI_6]$, which can be arranged as a single octahedron or a as a corner-sharing octahedra, and it is surrounded by randomly oriented solvent molecules. It is shown that the fraction of the core depends on the solvent used, solvents with high DN i.e. NMP or DMSO favour the single octahedron arrangement whereas GBL favours the corner-sharing octahedra arrangement. The scattering objects were modelled as spheres, which can be polydisperse or monodisperse. The structural analysis of the SAXS data also shows that the samples synthesised with GBL present higher polydispersity, whereas the samples synthesised with a high fraction of DMSO are monodisperse. These results are in agreement with the proposed core-shell model. The interaction of the scattering objects (structure factor) was modelled as hard spheres. This model works under the assumption that the scattering objects are not compressible and they cannot penetrate each other; it is described mainly by the radius of the hard sphere (R_{HS}), which is the minimum distance between the scattering objects. It is possible to explain the R_{HS} by assuming the smallest arrangement in the core, which the single octahedron, surrounded by oriented solvent molecules. The model proposed in this chapter does not consider the A-cation since, as it will be shown in Chapter 6, organic A-cations do not have an influence in the arrangement of the scattering objects.

Chapter 5. Influence of the halide in the early stage of crystallisation of hybrid halide perovskites: application of the core-shell model

This chapter shows the effect of the anion in the atomic arrangement when the I^- is exchanged for Br^- or Cl^- in $MAPbI_3$ precursor solution.

5.1. $MAPbBr_3$ precursor solution

$MAPbBr_3$ precursor solutions synthesised with DMF and DMF:DMSO 50:50 as solvents were analysed with SAXS. The experimental distance obtained from the peak position is 1.718±0.020 and 2.673±0.020 nm, respectively. Interestingly, the d_{exp} obtained for $MAPbBr_3$ in DMF:DMSO 50:50 is much bigger than the one obtained for the solution made with DMF. Comparing the core fractions of $MAPbI_3$ and $MAPbBr_3$ in DMF (Figure 5.1), it can be concluded that exchanging the I^- for Br^- favours the single core arrangement. Taking that into consideration, the difference in size between $MAPbBr_3$ in DMF and in DMF:DMSO 50:50 can be explained if the scattering objects are surrounded by 2 solvent molecules instead of one (Figure 5.2). The d_{exp} can be described by equation 5.1.

$$d_{model} = 2 \cdot r_{core} + 8 \cdot \bar{r}_s \tag{5.1}$$

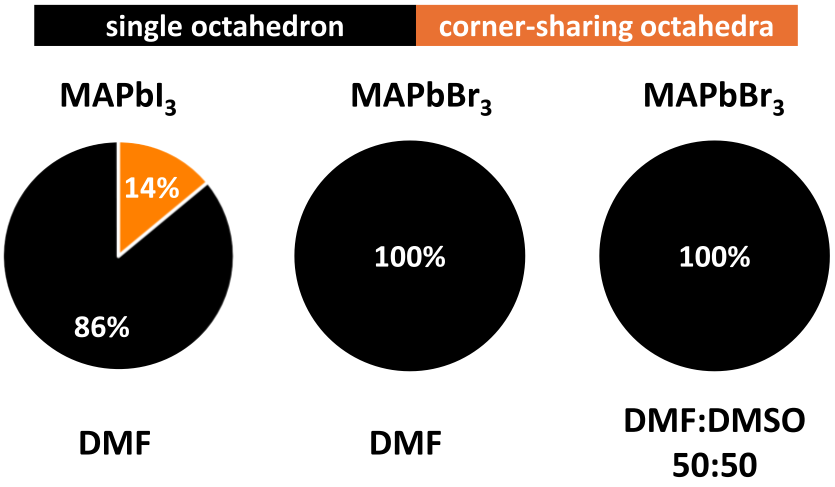

Figure 5.1. Core fractions of $MAPbBr_3$ precursor solution in DMF and DMF:DMSO 50:50 compared to $MAPbI_3$ in DMF.

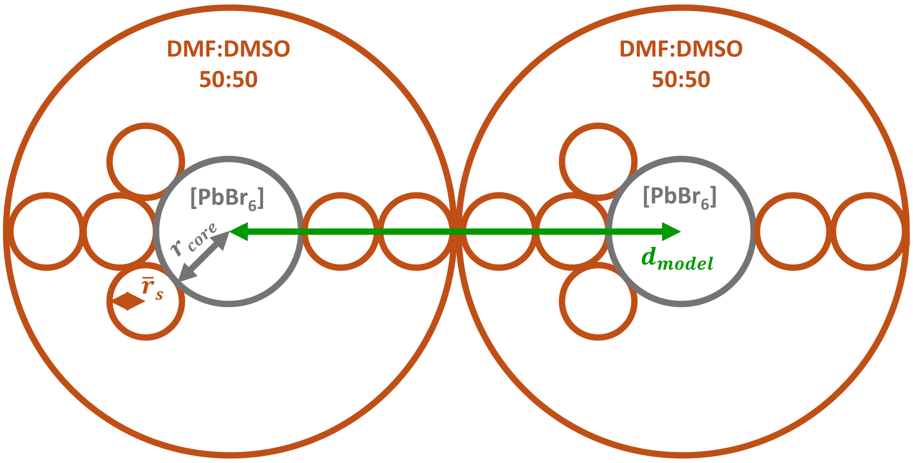

Figure 5.2. Core-shell model for $MAPbBr_3$ in DMF:DMSO 50:50. Each scattering object is formed by a $[PbBr_6]^{4-}$ single octahedron and 2 rows of randomly oriented solvent molecules around it.

The structural information was obtained by fitting the SAXS patterns to a model-based form factor. The shape of the scattering objects was modelled as spheres. The SAXS analysis shows that in both cases, the solutions are monodisperse, which is in agreement with the proposed core-shell model. Moreover, the radius of the spheres obtained from the fits was 0.293 and 0.278 nm, which is approximately the Pb-Br bond length 0.288 nm.

The interaction between the scattering objects was modelled as a hard sphere. The radius of the hard sphere obtained for $MAPbBr_3$ synthesised in DMF and in DMF:DMSO 50:50 was

0.675 and 1.265 nm, respectively. Since both samples are formed by the smallest core arrangement, the minimum distance between scattering objects can be explained by having oriented solvent molecules around the core. However, the number of solvent molecules between the cores differs. In the case of $MAPbBr_3$ precursor solution synthesised with DMF, the R_{HS} can be explained by having one solvent molecule between two cores (equation 5.2). On the other hand, R_{HS} for $MAPbBr_3$ synthesised with DMF:DMSO 50:50 can be explained by having 4 solvent molecules between the cores (equation 5.3), which follows the same trend as d_{exp}.

$$R_{HS} = r_{core}^{single} + r_s^{app} \tag{5.2}$$

$$R_{HS} = r_{core}^{single} + 4r_s^{app} \tag{5.3}$$

Despite having DMSO a higher donor number than DMF and, therefore, a higher coordinating ability, these results show that including DMSO in the $MAPbBr_3$ precursor solution produces the opposite effect. It was shown that the scattering objects in the solution do not increase in size but they grow apart due to having more solvent molecules between them.

5.2. $MAPbCl_3$ precursor solution

$MAPbCl_3$ precursor solution synthesised with DMF:DMSO 50:50 as solvent was analysed with SAXS. Interestingly, the SAXS pattern obtained from the measurement did not show any peak, which translates to the lack of agglomeration in the solution. Comparing the SAXS patterns of $MAPbI_3$ and $MAPbBr_3$ with $MAPbCl_3$ in DMF:DMSO 50:50 and the solvent alone (Figure 5.3), it can be seen how the SAXS peak is less pronounced when Br^- is used as a halide, and it disappears completely when the halide is exchanged for Cl^-. This indicates that not only the solvent is an important criterion for the agglomeration of the precursors in solution, but the halide also plays an important role. Moreover, while it has been reported that the crystallisation of $MAPbI_3$ in DMF and in DMSO undergoes through intermediates,[80] the same cannot be said about $MAPbBr_3$ and $MAPbCl_3$.

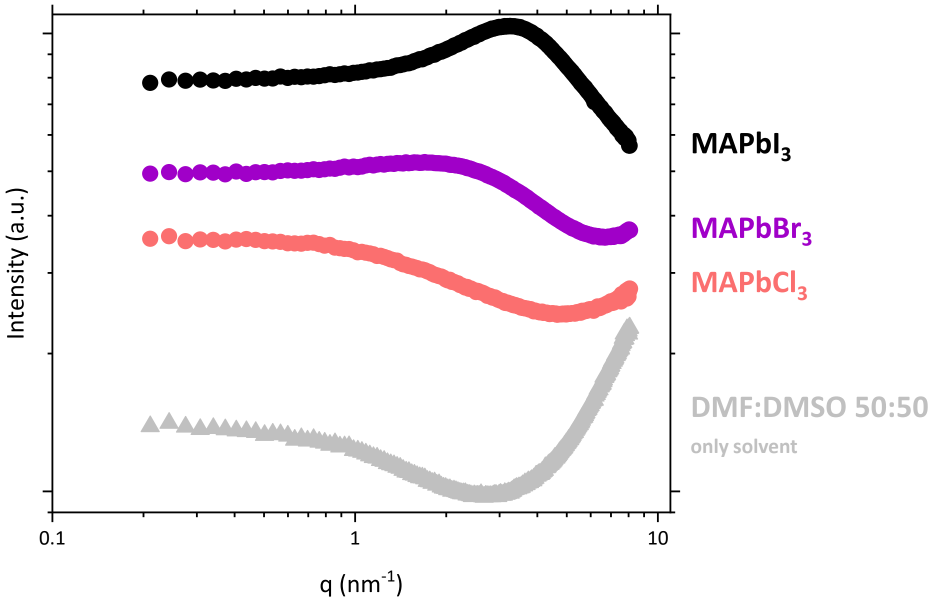

Figure 5.3. SAXS patterns of $MAPbI_3$ (black), $MAPbBr_3$ (purple), $MAPbCl_3$ (pink) precursor solutions and DMF:DMSO 50:50 (grey).

Unfortunately, it was not possible to fit the $MAPbCl_3$ SAXS pattern to determine the form factor due to the low scattering power of $MAPbCl_3$.

5.3. Conclusions

In order to understand the role of the halide in the hybrid halide perovskite early stage crystallisation, $MAPbBr_3$ precursor solution synthesised in DMF and in DMF:DMSO 50:50, as well as $MAPbCl_3$ precursor solution synthesised in DMF:DMSO 50:50, were investigated with SAXS. Comparing the results obtained for $MAPbI_3$, $MAPbBr_3$ an $MAPbCl_3$ synthesised in DMF:DMSO 50:50, it can be concluded that the role of the halide is crucial for the stability of the agglomerates in solution. $MAPbI_3$ precursor solution shows a sharp peak indicating the presence of interacting scattering objects. However, the peak is less noticeable when bromide is used as a halogen and, finally, non-existent when chloride is used instead. Comparing the results obtained for $MAPbBr_3$ precursor solution synthesised in DMF and in

DMF:DMSO 50:50, it was found that in both cases, the scattering objects are approximately the size of the Pb-Br bond length. Despite having roughly the same size, the distance between the scattering objects in both samples is very different. This can be explained by having four randomly oriented solvent molecules between the core of the scattering objects. Moreover, it was found that the use of Br^- as a halide favours the single octahedron arrangement in the core. The SAXS pattern corresponding to $MAPbCl_3$ in DMF:DMSO 50:50 did not show any peak. Compared to the SAXS pattern of DMF:DMSO 50:50 (only the solvent without any precursors), it can be seen that they have the same shape, showing the lack of interacting scattering objects in the solution. Unfortunately, it was not possible to fit the $MAPbCl_3$ pattern to determine the size and shape of the scattering objects. This could be due to the low scattering power of $MAPbCl_3$.

Chapter 6. Influence of the A-cation in the early stage of crystallisation of hybrid halide perovskites

This chapter shows the effect of the A-cation in the arrangement of the scattering objects in solution. Alkali metals (Na^+, K^+, Rb^+ and Cs^+) were used as inorganic *A*-cations, and FA^+ was used as organic *A*-cations.

6.1. Case of inorganic *A*-cation (Na^+, K^+, Rb^+, Cs^+) compared to organic *A*-cations (FA^+, MA^+) in *A*PbI_3

In order to understand what the role of the *A*-cation is in the early stage crystallisation, halide perovskite precursor solutions with organic (MA^+, FA^+) and inorganic (Na^+, K^+, Rb^+ and Cs^+). All the solutions were synthesised using GBL, GBL:DMF 50:50 and DMF as solvents, except $CsPbI_3$, which was synthesised using DMF:DMSO 80:20. When $CsPbI_3$ precursor solution was synthesised with GBL and GBL:DMF 50:50, the solution turned into a yellow gel-like consistency, for this reason, the solvent was changed.

The experimental distance of all the studied solutions was determined based on the peak position of the SAXS pattern (Figure 6.1). The obtained d_{exp} vary not only with the solvent, as shown for $MAPbI_3$ and $MAPbBr_3$ in Chapter 4 and Chapter 5, but also with the halide composition. The experimental distance for the samples synthesised with DMF is lower than the d_{exp} obtained for the samples synthesised with GBL. This phenomenon is expected because DMF has higher DN, preventing the precursors from forming large iodoplumbates in solution.

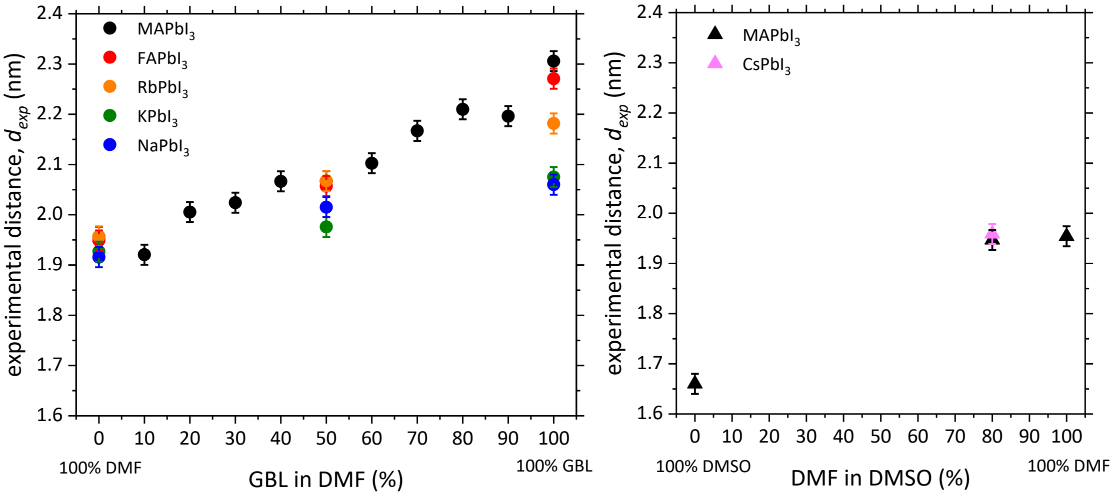

Figure 6.1. Experimental distance calculated from the peak position for the samples prepared with GBL, and DMF mixtures (left) and DMF:DMSO mixture (right).

When the nature of the *A*-cation is compared, i.e. organic or inorganic, it can be observed that d_{exp} of MAPbI$_3$ and FAPbI$_3$ do not differ significantly despite the difference in size of MA$^+$ and FA$^+$, (0.217 and 0.253 nm respectively).[81] Regarding the samples with inorganic *A*-cation, the difference in the d_{exp} cannot be explained solely by the difference in the *A*-cation (and solvent) size. Since the core-shell model proposed in Chapter 4 cannot explain these differences, because it does not take into consideration the *A*-cation, an extended core-shell model was developed.

6.2. Extension of the core-shell model

Since the d_{exp} changes not only with the solvent but also with the size of the inorganic *A*-cation, the previous core-shell model was extended to include the *A*-cation (Figure 6.2). The scattering objects in hybrid halide perovskites precursor solutions with an organic *A*-cation are described with the previous core-shell model since it was demonstrated that the choice of organic *A*-cation does not affect the distance between the scattering objects.

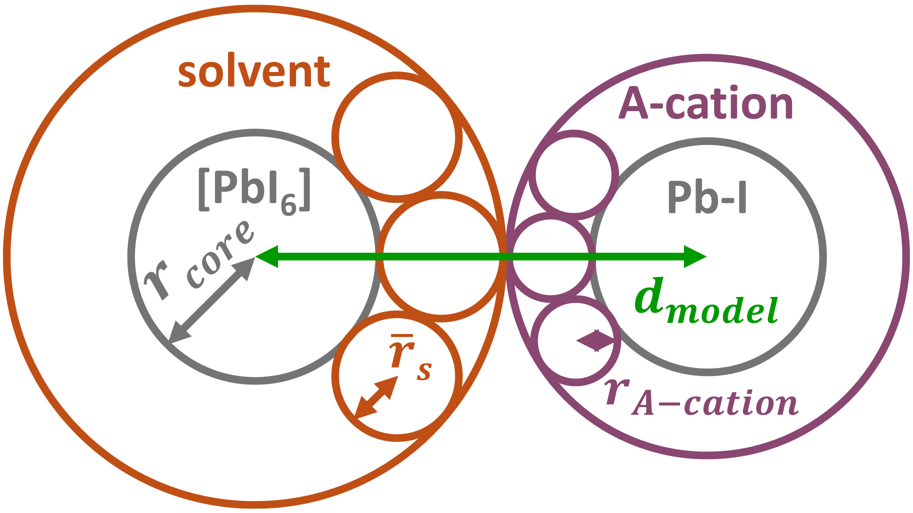

Figure 6.2. Scheme of the extended core-shell model. The [PbI_6] octahedra core, which can be arranged as a single octahedron ([PbI_6]$^{4-}$) or as corner-sharing octahedra ([Pb_2I_{11}]$^{7-}$), is surrounded by randomly oriented solvent molecules or by an inorganic A-cation. The distance between the centre of mass between the scattering objects is shown as d_{model}.

As with the previous core-shell model, the core can be arranged as a single octahedron [PbI_6]$^{4-}$ or as a corner-sharing octahedra [Pb_2I_{11}]$^{7-}$. The core is surrounded not only by randomly oriented solvent molecules but also by inorganic *A*-cation. The modelled distance can be described with equation 6.1,

$$d_{model} = 2r_{core} + 2\bar{r}_s + 2r_{A-cation} \qquad 6.1$$

where r_{core} is the radius of the core (described by equations 4.3 and 4.4), $\bar{r}_s$ is the geometrical mean of the solvent molecules modelled as ellipsoids (Table 4.1) and $r_{A-cation}$ is the radius of the inorganic *A*-cation (Table 6.1).

Table 6.1. Radii of the inorganic cations used for the extended model.[82]

cation	**radius (nm)**
Cs^+	0.188
Rb^+	0.172
K^+	0.164
Na^+	0.139

At first sight, it is evident that there is a difference between the core fraction of the samples with organic *A*-cation and the samples with inorganic *A*-cation (Figure 6.3). In all the solvent or solvent combinations, the single octahedron core is lower for the samples with inorganic *A*-cation, therefore it can be concluded that the inorganic *A*-cation favours the corner-sharing octahedra arrangement. These results also highlight the fact that solvents with lower DN (GBL) produce larger iodoplumbates in solution (corner-sharing octahedra) compared to DMF or DMSO, which form a higher amount of single octahedra in solution.

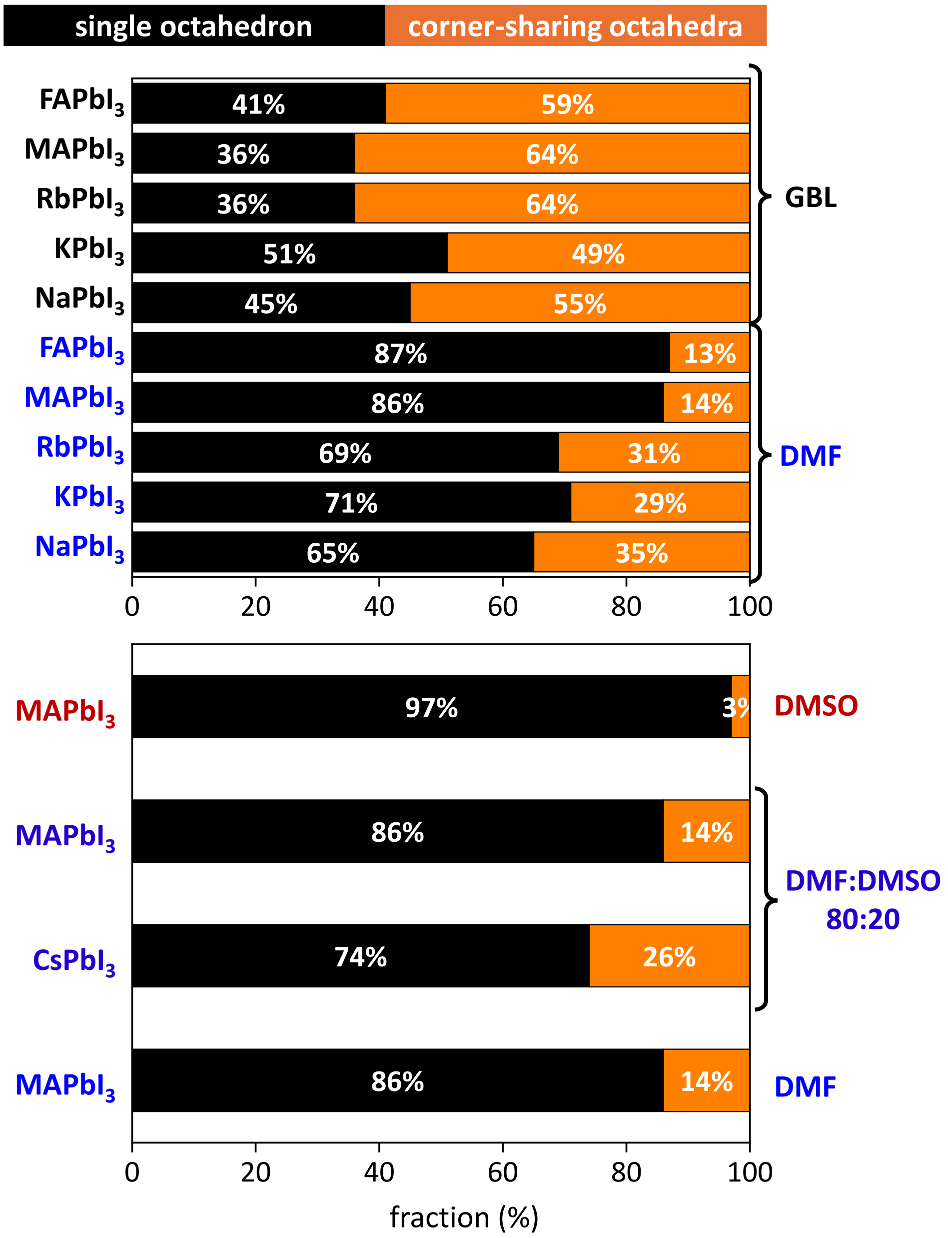

Figure 6.3. Proportion of single octahedra (black) and corner-sharing octahedra (orange) in the core.

6.3. Polydispersity and charge distribution

The structural information was obtained by fitting the SAXS patterns to a model-based form factor. The shape of the scattering objects was modelled as spheres. As expected from the obtained core fractions, all the studied samples show polydispersity (Figure 6.4). The polydispersity index of the samples with inorganic *A*-cation is higher than the ones with organic *A*-cation. This can be explained by having more different scattering objects in solution. While all samples contain the same elements (*A*-cation, B-cation, solvent and X-anion), only the inorganic *A*-cations interact with the core, forming a core-shell species. This is related to the charge density of the alkali cations; since they are much smaller than the organic A-cations, they are more drawn to the highly negative core.

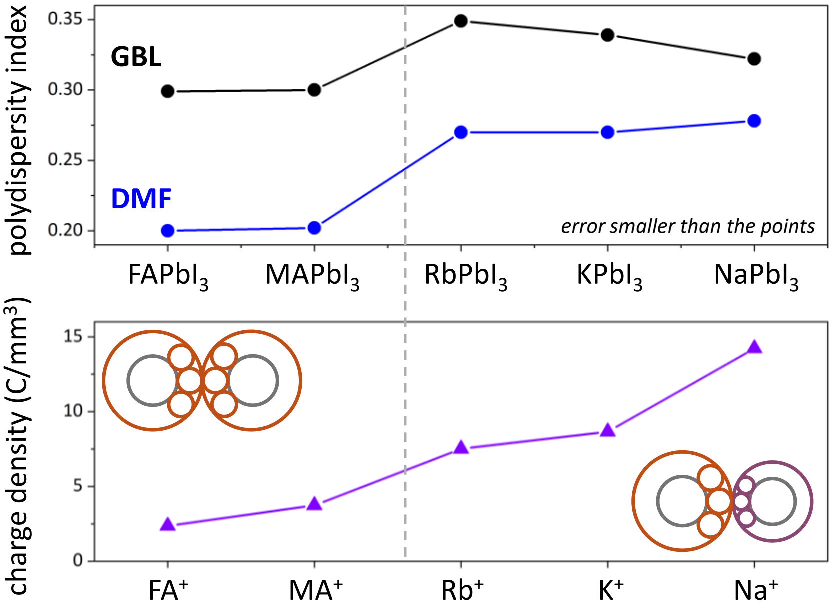

Figure 6.4. Polydispersity index obtained from the fit for A-cation substituted halide perovskite precursor solutions (top) compared to the charge density of the respective A-cations (bottom).

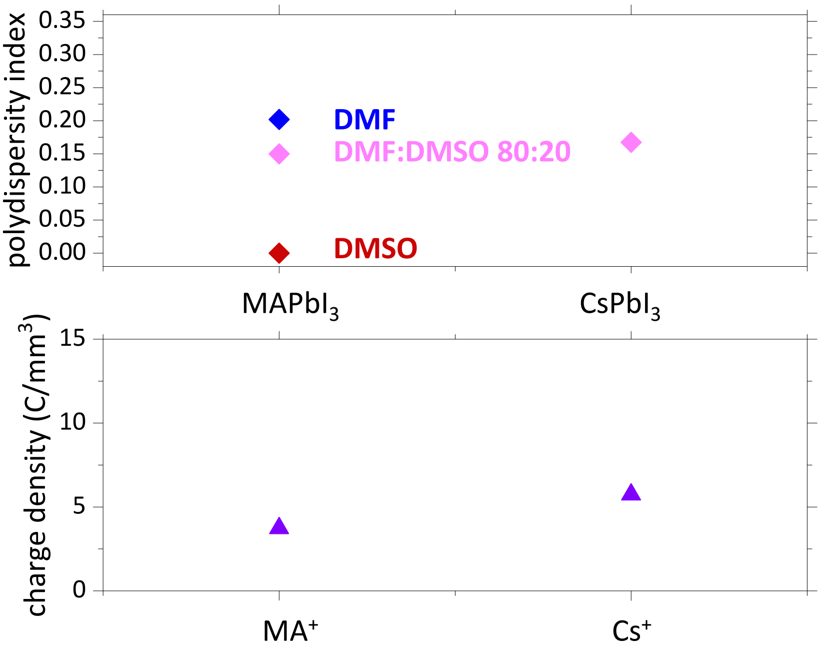

Figure 6.5. Polydispersity index of $CsPbI_3$ in DMF:DMSO 80:20 compared to $MAPbI_3$ in DMF, DMSO and DMF:DMSO 80:20 (top), charge density of Cs^+ compared to MA^+ (bottom).

The polydispersity index of $CsPbI_3$ precursor solution in DMF:DMSO 80:20 is a bit higher than the polydispersity index of $MAPbI_3$ in DMF:DMSO 80:20 (Figure 6.5), which is in agreement with the core fractions obtained from the core-shell model.

6.4. The model of the hard sphere radius

The interaction between the scattering objects was modelled as a hard sphere. The radius of the hard sphere, which is the minimum distance between the scattering objects, was calculated by considering the smallest arrangement possible in the core (single octahedron) and oriented solvent molecules around the core (equation 4.5). For the samples with inorganic A-cation, R_{HS} can be explained with equation 6.2,

$$R_{HS} = r_{core}^{single} + r_s^{app} + r_{A-cation} \qquad 6.2$$

where the minimum distance is considered to be one r_{core}, the radius of the oriented solvent molecule and the radius of the *A*-cation. In this case, a solvent molecule and an alkali metal cation are assumed to be included in the minimum distance. R_{HS} can be explained for all the samples synthesised with GBL:DMF with an oriented solvent molecule (Figure 6.6).

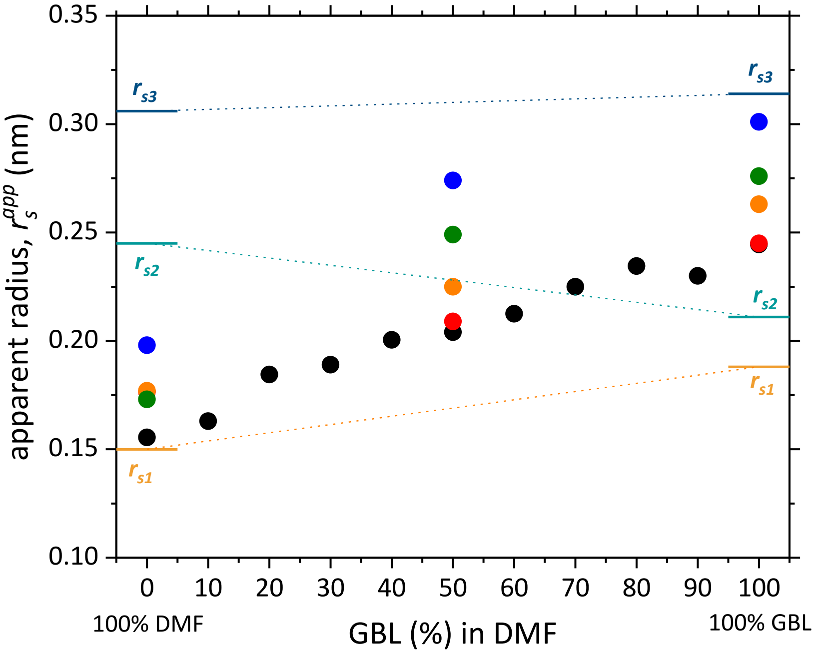

Figure 6.6. Apparent radius of $APbI_3$ with A = MA, FA, Na, K and Rb precursor solutions using GBL, GBL:DMF 50:50 and DMF as solvents. The dotted lines are only to guide the eyes.

However, in the case of $CsPbI_3$, it is not possible to justify the minimum distance using the same procedure. The distance calculated using r_{core}^{single}, an oriented solvent molecule and the Cs^+ radius is too big compared to the R_{HS}. In this case, it is possible to explain the minimum distance between the scattering objects if either one solvent molecule or the *A*-cation is placed between two cores. This is described in equation 6.3.

$$R_{HS} = r_{core}^{single} + 0.5r_{s}^{app} + 0.5r_{A-cation} \tag{6.3}$$

6.5. Conclusions

In this chapter, halide perovskites precursor solutions with different *A*-cations were studied with SAXS to understand how the *A*-cation impacts the arrangement of the scattering objects in solution. It was shown that the nature of the *A*-cation influences the arrangement of the scattering objects. Organic *A*-cations do not interact with the core, therefore the core is only surrounded by randomly oriented solvent molecules. On the other hand, when the *A*-cation is inorganic, the cores are surrounded by randomly oriented solvent molecules and by the inorganic *A*-cation. Comparing the results of the core fractions obtained for the samples with inorganic *A*-cation and the core fractions obtained with the organic *A*-cation, it is clear that the inorganic *A*-cation favours the formation of the corner-sharing octahedra arrangement. The structural data obtained from SAXS shows that the samples with an inorganic *A*-cation present higher polydispersity than the ones with an organic *A*-cation, which is in agreement with the extended core-shell model. Finally, the radius of the hard sphere can be explained by considering oriented solvent molecules as well as the alkali metal. In the case of the $CsPbI_3$ precursor solution, the minimum distance between scattering objects can be explained by having only one solvent molecule or the Cs^+ cation between the cores.

Chapter 7. Investigation of the atomic arrangement in the precursor solution and structural changes of $MAPbI_3$ in long-time experiments

This chapter is focused on the ageing of $MAPbI_3$ precursor solution and $MAPbI_3$ powder. The precursor solutions were investigated with SAXS for 132 weeks, whereas the powder samples were investigated for 151 weeks with XRD.

7.1. Ageing of $MAPbI_3$ precursor solutions through 132 weeks

One of the major drawbacks of HHPs is their low long-term stability. However, very little is known about the stability of the precursor solution. The precursor solutions synthesised for the study shown in Chapter 4 were remeasured through 132 weeks (31 months) to understand how the solution ages over time (Figure 7.1).

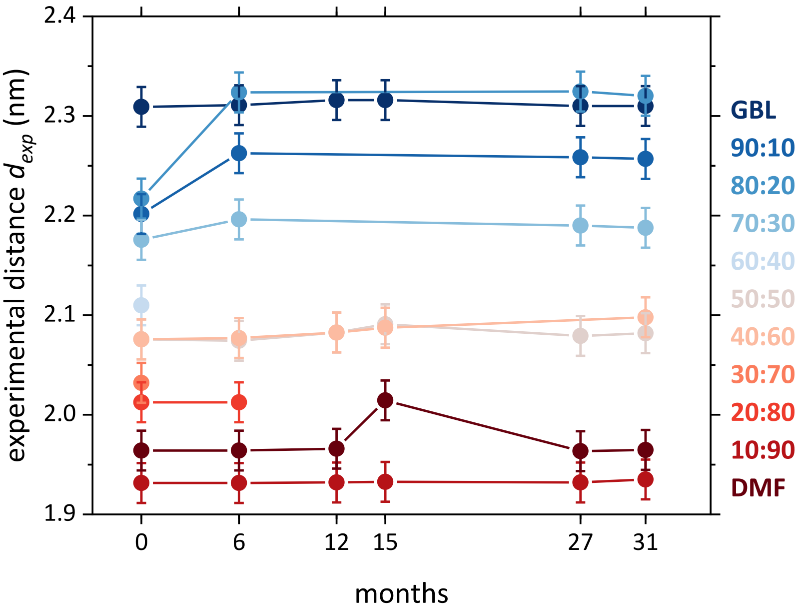

Figure 7.1. Experimental distance for $MAPbI_3$ precursor solutions in GBL:DMF through 132 weeks.

Most samples do not show a significant difference in the distance between the scattering objects when the first and last measurements are compared. Nevertheless, the precursor solutions synthesised with the GBL:DMF ratios 70:30, 80:20 and 90:10 showed crystal growth within the capillaries (Figure 7.2). The crystal growth occurred during the first 6 months and did not develop any further.

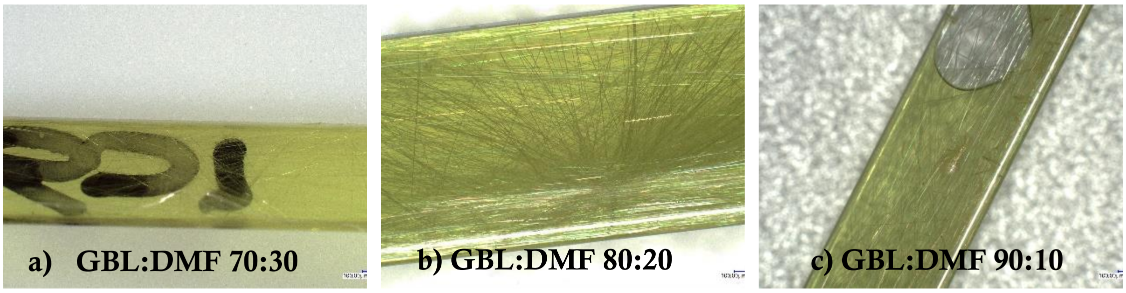

Figure 7.2. Microscopy image of $MAPbI_3$ precursor solution in different GBL:DMF solvent ratios showing crystal growth. a) $MAPbI_3$ precursor solution prepared in GBL:DMF 70:30. b) $MAPbI_3$ precursor solution prepared in GBL:DMF 80:20. c) $MAPbI_3$ precursor solution prepared in GBL:DMF 90:10.

The crystals show a needle-like morphology, indicating that they could be an intermediate with DMF.[63] Further investigation of these crystals is needed to determine their composition.

The morphology of the scattering objects remained the same as the freshly synthesised samples, all the samples were modelled as spheres. The median of the size distribution was fixed at 0.319 nm, which is the Pb-I bond length. The interaction between the scattering objects was modelled as a hard sphere.

7.2. Ageing of $MAPbI_3$ through 151 weeks in air

Two $MAPbI_3$ samples were synthesised in order to study the long-term stability of the bulk samples. One sample was kept in an air-tight dome, whereas the other was open to the atmosphere (Figure 7.3). The sample with the air-tight dome was assembled in air. Both samples were measured weekly using XRD for 28 weeks. The samples were kept in a cabinet, and they were remeasured again after 122 and 151 weeks (2.4 and 2.9 years, respectively. Figure 7.4).

Figure 7.3. Freshly synthesised $MAPbI_3$.

Figure 7.4. $MAPbI_3$ after 151 weeks stored in air.

The sample kept in air shows evident signs of $MAPbI_3$ degradation. The top layer of the sample decomposed to PbI_2. On the other hand, the sample in the air-tight dome only shows evidence of PbI_2 at the rim of the sample holder. Most of the surface remains in the α-phase from $MAPbI_3$. The XRD diffractogram of the sample kept in the air-tight dome (Figure 7.5) does not show evidence of PbI_2 formation until week 16, 4 months after synthesis. PbI_2 presence is evident due to the appearance of the characteristic Bragg peaks at 12.70, 25.94, 34.28 and 39.5°, among others. This experiment shows the potential of HHP encapsulation since it is possible to avoid the degradation of $MAPbI_3$ to PbI_2 for up to 4 months.

The XRD diffractogram of the sample kept open to the atmosphere (Figure 7.6) shows that the degradation of $MAPbI_3$ to PbI_2 occurs much earlier than in the previous sample. In this case, the sample shows signs of PbI_2 presence since week 1. The main PbI_2 Bragg peaks at 12.7 and 25.94° increased significantly more than in the previous sample, while the main $MAPbI_3$ Bragg peaks decreased simultaneously.

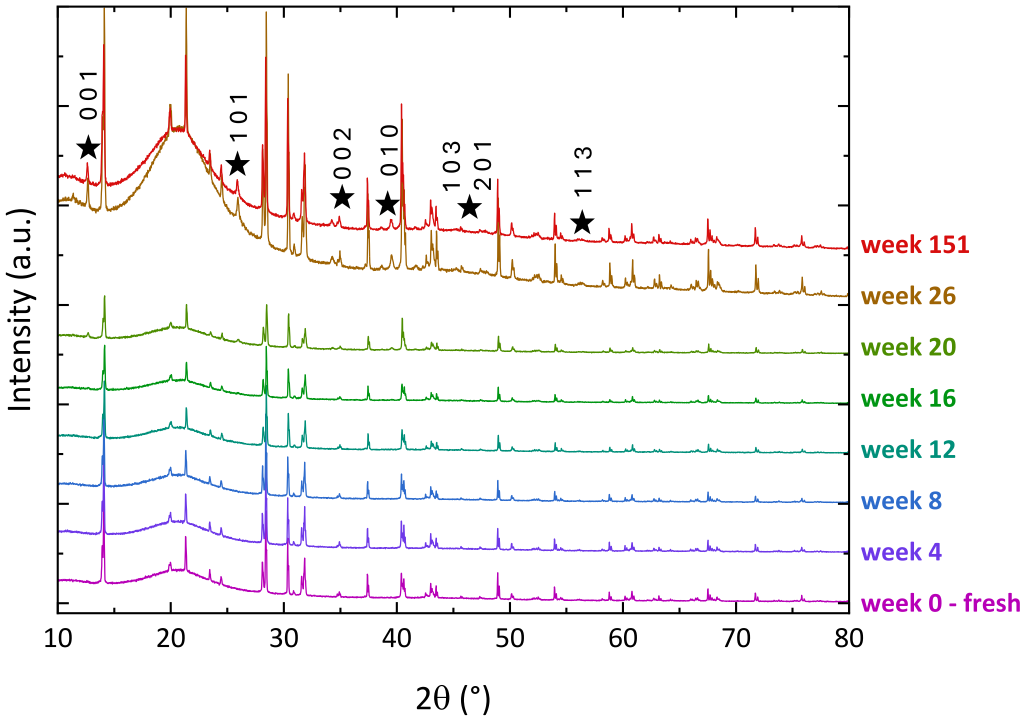

Figure 7.5. XRD pattern of $MAPbI_3$ kept in an air-tight dome for 151 weeks. PbI_2 Bragg peaks are highlighted with a star.

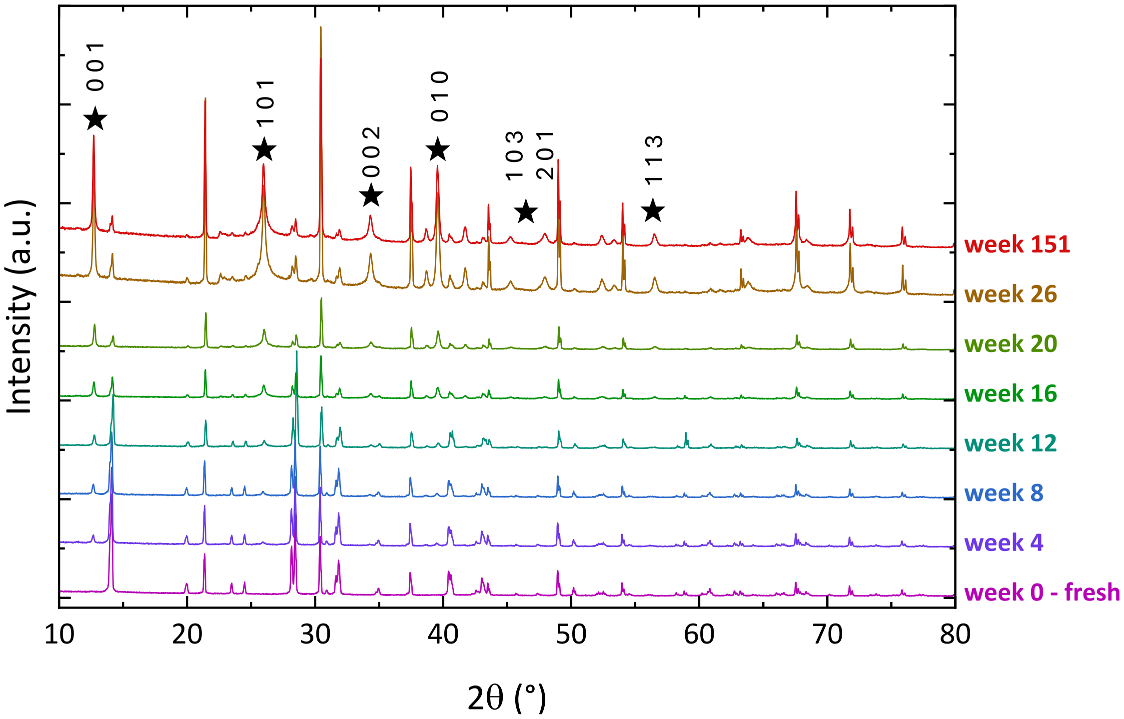

Figure 7.6. XRD pattern of $MAPbI_3$ open to the air through 151 weeks. PbI_2 Bragg peaks are highlighted with a star.

7.3. Conclusions

This chapter shows a long-time experiment in which $MAPbI_3$ precursor solutions were measured with SAXS for up to 132 weeks (2.4 years). Most of the samples do not show changes in the experimental distance, and therefore not in the core arrangement proportion, except for the samples synthesised with the solvent ratios GBL:DMF 70:30, 80:20 and 90:10. Within 6 months, the aforementioned samples showed crystal growth in the form of yellow needle-like crystals. Further investigation of the crystals must be performed in order to determine their composition. It can be concluded that $MAPbI_3$ precursor solutions in different GBL:DMF ratios are stable over time, except for those specific solvent ratios. Furthermore, the aged samples did not show changes in the size, shape or interaction between the scattering objects,

Two polycrystalline samples were synthesised, and while one of them was kept in an air-tight dome, the other was exposed to the air. The sample open to the atmosphere showed signs of degradation after the first week, whereas the sample in the air-tight dome was phase pure for 16 weeks. The intensity of the Bragg peaks corresponding to $MAPbI_3$ decreased substantially as opposed to the Bragg peaks assigned to PbI_2 for the sample open to the atmosphere, which is in agreement with the sample colour change due to $MAPbI_3$ degradation.

Chapter 8. Summary and outlook

Hybrid halide perovskites are promising materials for solar cells, having achieved 26.7% PCE in 2024. Whether HHPs are processed as thin films,[83] bulk[20] or single crystals,[84] the synthesis from solution remains the most popular method. Despite this popularity, the formation mechanism of this material from solution is not well understood. This dissertation aims to shed some light on the topic, especially on how the precursors are arranged in the solution at the early stage of crystallisation. Three main topics are covered: the effect of the solvent, the effect of the anion and the effect of the A-cation.

Firstly, to investigate the effect of the solvent, $MAPbI_3$ precursor solutions were synthesised in GBL, DMF, NMP, DMSO and mixtures thereof. The precursor solutions were investigated with SAXS in order to obtain more information about the morphology and interaction of the scattering objects in solution. The distance between scattering objects (d_{exp}) obtained from the SAXS pattern peak position can be explained by a core-shell model, where the core is formed by $[PbI_6]$, which can be arranged as a single octahedron or as corner-sharing octahedra. It was demonstrated that the use of a solvent with low Gutmann's donor numbers (e.g. GBL) favours the corner-sharing octahedra arrangement. This is due to the low coordinating power with Pb^{2+}, which in turn is more accessible to bond with I^-. It was shown that there is a correlation between the DN of a solvent and the d_{exp} between the scattering objects, where high DN lead to lower d_{exp}. Comparing the core-shell model with the structural information obtained from SAXS, it was shown that solvents with high DN (NMP, DMSO) tend to form monodisperse solutions, which is in agreement with the core-shell model.

The effect of the anion was investigated by analysing the precursor solutions of $MAPbI_3$, $MAPbBr_3$ and $MAPbCl_3$ in DMF:DMSO 50:50 with SAXS. The characteristic peak indicating the presence of interaction between scattering objects is less noticeable when the I^- is substituted for Br^-, and it completely disappears when Cl^- is used as a halide instead. This is an indication that smaller halides are more affected by the effect of a coordinating solvent mixture such as DMF:DMSO since it prevents the formation of iodoplumbates in solution.

The effect of the cation was investigated by analysing $APbI_3$ precursor solution, with A = MA^+, FA^+, Na^+, K^+, Rb^+ and Cs^+ synthesised in GBL, GBL:DMF 50:50, DMF and DMF:DMSO 80:20 (only $CsPbI_3$). The experimental distance obtained from the SAXS patterns showed that while organic *A*-cation does not affect the arrangement of the scattering objects in solution, the same cannot be said about the inorganic *A*-cation. For this reason, an extended core-shell model was developed. In this model, the core is formed by PbI_6, which can be arranged as a single octahedron or as corner-sharing octahedra. The core is surrounded not only by randomly oriented solvent molecules but also by inorganic *A*-cation. This can be explained by the high charge density in alkali metals. The alkali metals are drawn towards the core since it is negatively charged. This translates into an increase in the polydispersity of the samples with inorganic *A*-cation.

Finally, an ageing experiment of bulk $MAPbI_3$, as well as an ageing experiment for $MAPbI_3$ precursor solutions, took place over 2 years. It was shown how the precursor solutions are stable over time since they are kept sealed in a capillary. Three specific solvent mixtures: GBL:DMF 70:30, 80:20 and 90:10, showed crystal growth after 6 months. Two samples of bulk $MAPbI_3$ were investigated over time; one of them was in an air-tight dome, while the other one was open to the atmosphere. The sample open to the atmosphere showed degradation evidence in less than a week. However, the sample sealed in an air-tight dome was phase pure for 4 months.

Although this study was focused on lead halide perovskites, it could be easily expanded to include other B-cations which are less toxic, such as Sn^{2+}, to determine whether tin-based perovskites follow the same crystallisation path. Due to the nature of the experiments, it is possible to investigate any HHPs composition as well as any solvent or solvent combination.

References

1. Causes and Effects of Climate Change. https://www.un.org/en/climatechange/science/causes-effects-climate-change.

2. Li, Y. *et al.* Suppressing Element Inhomogeneity Enables 14.9% Efficiency CZTSSe Solar Cells. *Adv. Mater.* **36**, 1–8 (2024).

3. Gao, J. *et al.* Over 19.2% Efficiency of Organic Solar Cells Enabled by Precisely Tuning the Charge Transfer State Via Donor Alloy Strategy. *Adv. Sci.* **9**, 1–8 (2022).

4. Best Research-Cell Efficiency Chart. https://www.nrel.gov/pv/cell-efficiency.html.

5. Kulkarni, S. A. *et al.* Band-gap tuning of lead halide perovskites using a sequential deposition process. *J. Mater. Chem. A* **2**, 9221–9225 (2014).

6. Our world in data: energy. https://ourworldindata.org/energy%0A.

7. First Practical Silicon Solar Cell. https://www.aps.org/apsnews/2009/04/bell-labs-silicon-solar-cell.

8. Shockley, W. & Queisser, H. J. Detailed Balance Limit of Efficiency of p-n Junction Solar Cells. *J. Appl. Phys.* **32**, 510–519 (1961).

9. Kojima, A., Teshima, K., Shirai, Y. & Miyasaka, T. Organometal halide perovskites as visible-light sensitizers for photovoltaic cells. *J. Am. Chem. Soc.* **131**, 6050–6051 (2009).

10. Yoshikawa, K. *et al.* Silicon heterojunction solar cell with interdigitated back contacts for a photoconversion efficiency over 26%. *Nat. Energy* **2**, 17032 (2017).

11. Rose, G. Beschreibung einiger neuen Mineralien des Urals. *Ann. Phys.* (1839).

12. Breternitz, J. & Schorr, S. What Defines a Perovskite? *Adv. Energy Mater.* **8**, (2018).

13. Momma, K. & Izumi, F. VESTA 3 for three-dimensional visualization of crystal, volumetric and morphology data. *J. Appl. Crystallogr.* **44**, 1272–1276 (2011).

14. Nandigana, P. *et al.* An ambient process for hole transport layer-free highly stable MAPbI3 by addition of MACl for efficient perovskite solar cells. *Energy Adv.* **3**, 442–450 (2024).

15. Yang, D. *et al.* 28.3%-efficiency perovskite/silicon tandem solar cell by optimal transparent electrode for high efficient semitransparent top cell. *Nano Energy* **84**, 105934 (2021).

16. Zhang, J. *et al.* Carrier Diffusion and Recombination Anisotropy in the $MAPbI_3$ Single Crystal. *ACS Appl. Mater. Interfaces* **13**, 29827–29834 (2021).

17. Chowdhury, T. A. *et al.* Stability of perovskite solar cells: issues and prospects. *RSC Adv.* **13**, 1787–1810 (2023).

18. Wagner, L. *et al.* The resource demands of multi-terawatt-scale perovskite tandem photovoltaics. *Joule* **8**, 1142–1160 (2024).

19. Saidaminov, M. I. *et al.* High-quality bulk hybrid perovskite single crystals within minutes by inverse temperature crystallization. *Nat. Commun.* **6**, (2015).

20. Dang, Y. *et al.* Bulk crystal growth of hybrid perovskite material $CH_3NH_3PbI_3$. *CrystEngComm* **17**, 665–670 (2015).

21. Rakita, Y. *et al.* Tetragonal $CH_3NH_3PbI_3$ is ferroelectric. *Proc. Natl. Acad. Sci. U. S. A.* **114**, E5504–E5512 (2017).

22. Saidaminov, M. I. *et al.* High-quality bulk hybrid perovskite single crystals within minutes by inverse temperature crystallization. *Nat. Commun.* **6**, 7586 (2015).

23. Röntgen, W. C. On a New Kind of Rays. *Nature* **53**, 274–276 (1896).

24. *Nobel Lectures, Physics 1901-1921.* (Elsevier Publishing Company, Amsterdam, 1967).

25. von Laue, M. Eine quantitative Prüfung der Theorie für die Interferenzerscheinungen bei Röntgenstrahlen. *Ann. Phys.* **346**, 989–1002 (1913).

26. Bragg, W. L. The structure of some crystals as indicated by their diffraction of X-rays. *Proc. R. Soc. London. Ser. A* **89**, 248–277 (1913).

27. Bragg, W. L. The Specular Reflection of X-rays. *Nature* **90**, 410–410 (1912).

28. Condition for the constructive interference of waves from a crystal film. https://virtuelle-experimente.de/en/elektronenbeugung/einfuehrung/bragg-bedingung.php.

29. Le Bail, A., Duroy, H. & Fourquet, J. L. Ab-initio structure determination of $LiSbWO_6$ by X-ray powder diffraction. *Mater. Res. Bull.* **23**, 447–452 (1988).

30. Rietveld, H. M. A profile refinement method for nuclear and magnetic structures. *J. Appl. Crystallogr.* **2**, 65–71 (1969).

31. Caglioti, G., Paoletti, A. & Ricci, F. P. Choice of collimators for a crystal spectrometer for neutron diffraction. *Nucl. Instruments* **3**, 223–228 (1958).

32. Nolze, G. PowderCell: a mixture between crystal structure visualizer, simulation and refinement tool. in *Powder diffraction. Proceedings of the II International School on Powder Diffraction* (eds. Sen Gupta, S. P. & Chatterje, P.) (Allied Publishers Limited, 2002).

33. Roisnel, T. & Rodriguez-Carvajal, J. WinPLOTR: a Windows tool for powder diffraction analysis. in *Materials Science Forum. Proceedings of the Seventh European Powder Diffraction Conference (EPDIC 7)* (eds. Delhez, R. & Mittenmeijer, E. J.) 118–123 (2000).

34. Zagorac, D., Muller, H., Ruehl, S., Zagorac, J. & Rehme, S. Recent developments in the Inorganic Crystal Structure Database: Theoretical crystal structure data and related features. *J. Appl. Crystallogr.* **52**, 918–925 (2019).

35. Glatter, O. & Kratky, O. *Small Angle X-Ray Scattering*. (Acade, 1982).

36. Schnablegger, H. & Singh, Y. *The SAXS Guide*. (Anton Paar, 2013).

37. Yang, Z., Gu, Q., Banjar, W., Li, N. & Hemar, Y. In situ study of skim milk structure changes under high hydrostatic pressure using synchrotron SAXS. *Food Hydrocoll.* **77**, 772–776 (2018).

38. Chen, D. & Ilavsky, J. Structural characterization of high-protein system through ultra-small and small-angle X-ray scattering. *Curr. Opin. Food Sci.* **59**, 101204 (2024).

39. Murthy, N. S. & Grubb, D. T. Evolution of elliptical SAXS patterns in aligned systems. *J. Appl. Crystallogr.* **57**, 1127–1136 (2024).

40. Shao, R. *et al.* SAXS unveils porous anodes for potassium-ion batteries: dynamic evolution of pore structures in $Fe@Fe_2O_3$/PCNFs composite nanofibers. *Phys. Chem. Chem. Phys.* **26**, 4885–4897 (2024).

41. Herrera, F., Rumi, G., Steinberg, P. Y., Wolosiuk, A. & Angelomé, P. C. Small Angle Scattering Techniques for the Study of Catalysts and Catalytic Processes. *ChemCatChem* **15**, (2023).

42. Bogar, M. *et al.* A small angle X-ray scattering approach for investigating fuel cell catalyst degradation for both ex situ and in operando analyses. *Int. J. Hydrogen Energy* **58**, 1673–1681 (2024).

43. Rudolph, B. *et al.* Nanoparticle Exsolution from Nanoporous Perovskites for Highly Active and Stable Catalysts. *Adv. Sci.* **10**, 1–12 (2023).

44. Hidalgo, J. *et al.* Solvent and A-Site Cation Control Preferred Crystallographic Orientation in Bromine-Based Perovskite Thin Films. *Chem. Mater.* **35**, 4181–4191 (2023).

45. Held, V. *et al.* Evolution of Defects, Morphology, and Strain during FAMAPbI$_3$ Perovskite Vacuum Deposition: Insights from In Situ Photoluminescence and X-ray Scattering. *ACS Appl. Mater. Interfaces* **16**, 35723–35731 (2024).

46. Guinier, A. & Fournet, G. *Small-Angle Scattering of X-Rays*. (John Wiley & Sons, Inc, 1955).

47. Feigin, L. A. & Svergun, D. I. *Structure Analysis by Small-Angle X-Ray and Neutron Scattering*. *Structure Analysis by Small-Angle X-Ray and Neutron Scattering* (Springer US, Boston, MA, 1987). doi:10.1007/978-1-4757-6624-0.

48. Percus, J. K. & Yevick, G. J. Analysis of Classical Statistical Mechanics by Means of Collective Coordinates. *Phys. Rev.* **110**, 1–13 (1958).

49. Vrij, A. Mixtures of hard spheres in the Percus-Yevick approximation. Light scattering at finite angles. *J. Chem. Phys.* **71**, 3267–3270 (1979).

50. Krumrey, M. & Ulm, G. High-accuracy detector calibration at the PTB four-crystal monochromator beamline. *Nucl. Instruments Methods Phys. Res. Sect. A Accel. Spectrometers, Detect. Assoc. Equip.* **467**, 1175–1178 (2001).

51. Hoell, A., Zizak, I., Bieder, H. & Mokrani, L. Einrichtung zur Kleinwinkelstreumessung zur Analyse der Nanostruktur an Proben mittels Röntgenstrahlung. (2007).

52. Wernecke, J., Gollwitzer, C., Müller, P. & Krumrey, M. Characterization of an in-vacuum PILATUS 1M detector. *J. Synchrotron Radiat.* **21**, 529–536 (2014).

53. Keiderling, U. The new 'BerSANS-PC' software for reduction and treatment of small angle neutron scattering data. *Appl. Phys. A Mater. Sci. Process.* **74**, 1455–1457 (2002).

54. Breßler, I., Kohlbrecher, J. & Thünemann, A. F. SASfit: A tool for small-angle scattering data analysis using a library of analytical expressions. *J. Appl. Crystallogr.* **48**, 1587–1598 (2015).

55. Peng, S. Y., Chuang, K. W., He, J. H. & Liao, Y. C. Direct Growth and Patterning of Single-Crystal Perovskites via Antisolvent Inkjet Printing. *ACS Appl. Electron. Mater.* **4**, 5468–5474 (2022).

56. Raj Mohan, S. *et al.* Static anti-solvent treatment on lead iodide in two-step deposition of methylammonium lead iodide perovskite thin films. *Opt. Mater. (Amst).* **147**, 114720 (2024).

57. Podapangi, S. K. *et al.* Green solvents, materials, and lead-free semiconductors for sustainable fabrication of perovskite solar cells. *RSC Adv.* **13**, 18165–18206 (2023).

58. Im, J. H., Lee, C. R., Lee, J. W., Park, S. W. & Park, N. G. 6.5% efficient perovskite quantum-dot-sensitized solar cell. *Nanoscale* **3**, 4088–4093 (2011).

59. Baikie, T. *et al.* Synthesis and crystal chemistry of the hybrid perovskite (CH_3NH_3)PbI_3 for solid-state sensitised solar cell applications. *J. Mater. Chem. A* **1**, 5628–5641 (2013).

60. Manser, J. S., Saidaminov, M. I., Christians, J. A., Bakr, O. M. & Kamat, P. V. Making and Breaking of Lead Halide Perovskites. *Acc. Chem. Res.* **49**, 330–338 (2016).

61. Petrov, A. A. *et al.* Formamidinium Haloplumbate Intermediates: The Missing Link in a Chain of Hybrid Perovskites Crystallization. *Chem. Mater.* **32**, 7739–7745 (2020).

62. Shargaieva, O. *et al.* Hybrid perovskite crystallization from binary solvent mixtures: interplay of evaporation rate and binding strength of solvents. *Mater. Adv.* **1**, 3314–3321 (2020).

63. Petrov, A. A. *et al.* Crystal Structure of DMF-Intermediate Phases Uncovers the Link Between $CH_3NH_3PbI_3$ Morphology and Precursor Stoichiometry. *J. Phys. Chem.* **121**, 20739–20743 (2017).

64. Fateev, S. A. *et al.* Solution Processing of Methylammonium Lead Iodide Perovskite from γ-Butyrolactone: Crystallization Mediated by Solvation Equilibrium. *Chem. Mater.* **30**, 5237–5244 (2018).

65. Huang, P. H., Wang, Y. H., Ke, J. C. & Huang, C. J. The effect of solvents on the performance of $CH_3NH_3PbI_3$ perovskite solar cells. *Energies* **10**, 599 (2017).

66. Radicchi, E., Mosconi, E., Elisei, F., Nunzi, F. & De Angelis, F. Understanding the Solution Chemistry of Lead Halide Perovskites Precursors. *ACS Appl. Energy Mater.* **2**, 3400–3409 (2019).

67. Wu, T. *et al.* Solvent engineering for high-quality perovskite solar cell with an efficiency approaching 20%. *J. Power Sources* **365**, 1–6 (2017).

68. Schlipf, J. *et al.* Top-Down Approaches Towards Single Crystal Perovskite Solar Cells. *Sci. Rep.* **8**, 1–8 (2018).

69. Gollino, L., Mercier, N. & Pauporté, T. Exploring Solar Cells Based on Lead- and Iodide-Deficient Halide Perovskite (d-HP) Thin Films. *Nanomaterials* **13**, 1–19 (2023).

70. Arteaga, J., Cherrette, V., Zhang, J. Z. & Ghosh, S. Complex Dependence of Optoelectronic Properties of Metal Halide Perovskite Thin Films on Quantum Dot Decoration Layers. *J. Phys. Chem. C* **127**, 17836–17842 (2023).

71. Gutmann, V. Solvent effects on the reactivities of organometallic compounds. *Coord. Chem. Rev.* **18**, 225–255 (1976).

72. Cataldo, F. A revision of the Gutmann donor numbers of a series of phosphoramides including TEPA. *Eur. Chem. Bull.* **4**, 92–97 (2015).

73. Rong, Y. *et al.* Solvent engineering towards controlled grain growth in perovskite planar heterojunction solar cells. *Nanoscale* **7**, 10595–10599 (2015).

74. Hamill, J. C., Schwartz, J. & Loo, Y. L. Influence of Solvent Coordination on Hybrid Organic-Inorganic Perovskite Formation. *ACS Energy Lett.* **3**, 92–97 (2018).

75. Palacios Saura, A., Breternitz, J., Hoell, A. & Schorr, S. The big bang of halide perovskites: The starting point of crystallization. *MRS Commun.* **14**, 711–716 (2024).

76. Breternitz, J. Solvent ellipsoids, Pb-X bond lengths and X^- radii calculations.

77. Flatken, M. A. *et al.* Small-angle scattering to reveal the colloidal nature of halide perovskite precursor solutions. *J. Mater. Chem. A* **9**, 13477–13482 (2021).

78. Viswamitra, M. A. & Kannan, K. K. Molecular dimensions and crystal structure of dimethyl sulphoxide at -60°C. *Nature* **209**, 1016–1017 (1966).

79. Brown, I. D. Structural chemistry and solvent properties of dimethylsulfoxide. *J. Solution Chem.* **16**, 205–224 (1987).

80. Petrov, A. A. *et al.* New Insight into the Formation of Hybrid Perovskite Nanowires via Structure Directing Adducts. *Chem. Mater.* **29**, 587–594 (2017).

81. Kieslich, G., Sun, S. & Cheetham, A. K. Solid-state principles applied to organic–inorganic perovskites: New tricks for an old dog. *Chem. Sci.* **5**, 4712–4715 (2014).

82. Shannon, R. D. Revised effective ionic radii and systematic studies of interatomic distances in halides and chalcogenides. *Acta Crystallogr. Sect. A* **32**, 751–767 (1976).

83. Yaghoobi Nia, N. *et al.* Solution-based heteroepitaxial growth of stable mixed cation/anion hybrid perovskite thin film under ambient condition via a scalable crystal engineering approach. *Nano Energy* **69**, (2020).

84. Yan, J. *et al.* Advances in the Synthesis of Halide Perovskite Single Crystals for Optoelectronic Applications. *Chem. Mater.* **35**, 2683–2712 (2023).

Conference contributions and publications

Conference contributions

Conference	Title, authors, contribution
BESSY II User Meeting 2021	Investigation of halide perovskite precursor solutions with SAXS A. Palacios Saura, J. Breternitz, A. Hoell, S. Schorr Poster presentation and lightning talk
5th German Conference for Research with Synchrotron Radiation, Neutrons and Ion Beams at Large Facilities (SNI2022)	Does the solvent matter? – Influence of the solvent in hybrid halide perovskites precursor solution A. Palacios Saura, J. Breternitz, A. Hoell, S. Schorr Poster presentation
2022 MRS Fall Meeting & Exhibit	Does the solvent matter? – Influence of the solvent in hybrid halide perovskites precursor solution A. Palacios Saura, J. Breternitz, A. Hoell, S. Schorr Oral presentation
31st Annual Meeting of the German Crystallographic Society (DGK 2023)	Does the solvent matter? – Influence of the solvent in hybrid halide perovskites precursor solution A. Palacios Saura, J. Breternitz, A. Hoell, S. Schorr Oral presentation
SAXS excites, International SAXS Symposium 2023	Does the solvent matter? – Influence of the solvent in hybrid halide perovskites precursor solution A. Palacios Saura, J. Breternitz, A. Hoell, S. Schorr Oral presentation
1st Helmholtz Energy Conference 2023	Does the solvent matter? – Influence of the solvent in hybrid halide perovskites precursor solution A. Palacios Saura, J. Breternitz, A. Hoell, S. Schorr Oral presentation
26th Congress and General Assembly of the International Union of Crystallography (IUCr 2023)	Does the solvent matter? – Influence of the solvent in hybrid halide perovskites precursor solution A. Palacios Saura, J. Breternitz, A. Hoell, S. Schorr Poster presentation – **poster prize**
6th International Conference on Perovskite Solar Cells and Optoelectronics (PSCO 2023)	Influence of the Precursors in Halide Perovskites Solutions A. Palacios Saura, J. Breternitz, A. Hoell, S. Schorr Oral presentation
1st Networking Workshop Seminar in the Helmholtz Topic Photovoltaics	Precursors Arrangement in the Early Stage of Halide Perovskites Crystallisation Process A. Palacios Saura, J. Breternitz, A. Hoell, S. Schorr Oral presentation
2023 MRS Fall Meeting & Exhibit	The Big Bang of Halide Perovskites: The Starting Point of Crystallisation

	A. Palacios Saura, J. Breternitz, A. Hoell, S. Schorr Poster presentation – **poster prize**
32nd Annual Meeting of the German Crystallographic Society (DGK 2024)	An Insight into Halide Perovskites Solutions: Precursors Arrangement Before Crystallisation A. Palacios Saura, J. Breternitz, A. Hoell, S. Schorr Poster presentation and lightning talk
1st PhD School on Perovskite PV	Investigation of Halide Perovskite Precursor Solutions with SAXS A. Palacios Saura, J. Breternitz, A. Hoell, S. Schorr Poster presentation
16th International Conference on Hybrid and Organic Photovoltaics (HOPV 2024)	Precrystallisation Arrangement in Halide Perovskites Precursor Solutions A. Palacios Saura, J. Breternitz, A. Hoell, S. Schorr Oral presentation

Publications

A. Palacios Saura, J. Breternitz, A. Hoell, S. Schorr, The Big Bang of Halide Perovskites: The Starting Point of Crystallization, MRS Commun., 2024, DOI: 10.1557/s43579-024-00611-x

A. Palacios Saura, J. Breternitz, A. Hoell, S. Schorr, Precrystallisation Arrangement in Halide Perovskites Precursor Solutions, International Conference on Hybrid and Organic Photovoltaics, 2024, DOI: 10.29363/nanoge.hopv.2024.035 (conference paper)

A. Palacios Saura, J. Breternitz, A. Hoell, S. Schorr, Does the Solvent Matter? – Influence of the Solvent in Hybrid Halide Perovskites Precursor Solution, Act Cryst. 2023, A79, C1149, DOI: 10.1107/S2053273323084723 (conference paper)